Porosity scaling strategies for low-*k* films

David J. Michalak,[a] James M. Blackwell, and Jessica M. Torres
Components Research, Intel Corporation, Hillsboro, OR 97124, USA

Arkaprabha Sengupta
Logic Technology Development, Intel Corporation, Hillsboro, OR 97124, USA

Lauren E. Kreno and James S. Clarke
Components Research, Intel Corporation, Hillsboro, OR 97124, USA

Daniel Pantuso
Logic Technology Development, Intel Corporation, Hillsboro, OR 97124, USA

(Received 17 August 2015; accepted 28 September 2015)

Reducing the delay of backend interconnects is critical in delivering improved performance in next generation computer chips. One option is to implement interlayer dielectric (ILD) materials with increasingly lower dielectric constant (*k*) values. Despite industry need, there has been a recent decrease in study and production of these materials in academia and business communities. We have generated a backbone and porogen system that allows us to control porosity from 0 to 60% volume, achieve *k*-values from 3.4 to 1.6, maintain high chemical stability to various wet cleans, and deliver uniquely high mechanical strength at a given porosity. Finite element modeling and experimental results demonstrate that further improvements can be achieved through control of the pore volume into an ordered network. With hopes to spur more materials development, this paper discusses some molecular design and nanoscale hierarchical principles relevant to making next generation low-*k* ILD materials.

I. INTRODUCTION

Integrated chip design over the past 5 decades has focused on physical size reduction for a number of reasons.[1,2] Transistors become faster and consume less power as they become smaller.[2] Manufacturing costs per chip also reduce as the number of chips on a production wafer increases. Building a higher performance chip at lower cost is a strong market driver for chip size reduction, but smaller than a certain minimum device size the challenges of design, integration, and yield rapidly increase costs. This interplay between manufacturing efficiency and production complexity means that for a given year there will be a minimum cost associated with integration of a certain number of components. Cited as "Moore's Law," Gordon Moore projected that the number of components associated with this minimum cost will double every 1–2 years,[3] and this projection has been the industry driven timeline for multiple decades.[3] But transistors aren't the only limiters of integrated circuit performance. Currently, the speed of integrated chips is more limited by signal delays in the wires that connect up transistors (also called the back-end interconnects) than the transistors themselves.[4] These delays are called *RC* delays because the amount of delay time, τ, is the product of resistance, *R*, and capacitance between neighboring lines, *C* ($\tau = RC$). Reducing the delay attributed to backend interconnects is therefore critical in delivering overall improved circuit performance in the next generation of computer chips. While the resistances, *R*, of the interconnect metal lines and vias are an active area of research and development, there are plenty of opportunities to improve delay by reducing the capacitance, *C*, of the interlayer dielectric (ILD) materials used to separate the metal lines. The capacitance, *C*, of a material that exists between two semi-infinite metal plates each having area, *A*, and separation, *d*, is given by

$$C = \frac{k\varepsilon_0 A}{d} \quad , \tag{1}$$

where *k* is the relative permittivity or dielectric constant of the ILD material and ε_0 is the permittivity of vacuum. While this semi-infinite model doesn't hold well for interconnect architectures due to increased fringing fields and additional complexity,[5,6] the equation above correctly represents that lowering the ILD *k*-value is the material engineer's only knob for reducing interconnect capacitance; the physical dimensions (*A* and *d* from the equation above) are constrained by design rules typically determined by size scaling. Next generation ILD materials will need to be carefully crafted to deliver a reduction in *k* while also

Contributing Editor: Paolo Colombo
[a]Address all correspondence to this author.
e-mail: david.j.michalak@intel.com
This paper has been selected as an Invited Feature Paper.
DOI: 10.1557/jmr.2015.313

 © Materials Research Society 2015

https://doi.org/10.1557/jmr.2015.313 Published online by Cambridge University Press

delivering needed mechanical and chemical stability properties. Many established avenues for k reduction have led to degradation of these properties.[4,7] The k-value is determined by:

$$\frac{(k-1)}{(k+2)} = \frac{N\alpha}{3\varepsilon_0} \quad , \tag{2}$$

where N is the number of polarizable units per volume, and α is that unit's polarizability described as:

$$\alpha = \alpha_e + \alpha_d + \alpha_o \quad , \tag{3}$$

which is the sum of electronic, distortion, and orientation polarizabilities. These principles as applied to ILDs have been reviewed extensively in the literature already.[4,6,8] The major points are that ILDs are typically composed of low-density materials (i.e., low N) and made from atoms of low atomic number (e.g., Si, C, O, N, H, and/or sometimes F) to reduce α_e.

Few manufacturable dense materials exhibit k-values less than 2.4; to target the International Technology Roadmap for Semiconductors (ITRS)[1] for backend dielectrics, ILD materials are deliberately made to have low densities.[9] When the density becomes low enough, the material becomes porous with pore sizes greater than 1 nm in size.[3] The Maxwell Garnett (MG) approximation[10] gives the functional form of the composite dielectric constant, k, when a dilute volume fraction, δ, of spherical inclusions of one material, k_1, is mixed into a host matrix of material with dielectric constant k_0.

$$k = k_0 \frac{k_1(1+2\delta) - k_0(2\delta - 2)}{k_0(2+\delta) + k_1(1-\delta)} \quad . \tag{4}$$

For a porous material having a dilute amount of spherical voids of vacuum ($k_1 = 1$) with porosity, $P = \delta$, the MG approximation simplifies to:

$$k = k_0 \frac{(1+2P) - k_0(2P-2)}{k_0(2+P) + (1-P)} \quad . \tag{5}$$

Due to their strength, thermal stability, and relatively low bulk polarizability, carbon-doped oxide "SiCOH" materials are often used as ILDs and have nonporous (k_0) values around 3.0–4.0.[11] To target effective dielectric constants below 2.2, these materials need to be fabricated to have porosities greater than 35–50% volume [Eq. (5)]. At these porosities, the pore structure is almost entirely interconnected.[12–15]

The integration of highly porous materials presents a number of challenges due to the reduced mechanical strength of porous networks[16] and the diffusion of materials (metals[17] or reactive etch gases[18–21]) into it. As an example, the left side of Fig. 1(a) shows a cross-sectional scanning electron microscope (SEM) image of the pattern fidelity after trench etch outlined by the yellow dotted line. Due to the porosity of the film, the highly reactive plasma etch gases diffused into the film and caused chemical damage (in the form of carbon depletion),[7,19,20,22] such that aqueous HF trench cleans etched away the C-depleted regions[23]; the resulting trench shape relative to the yellow line highlights the isotropic diffusion/damage profile of the etch gas species. If the damage is severe enough, profiles can start to delaminate [Fig. 1(a)].[24] Figure 1(b) shows a tilted cross-sectional SEM image after trench etch, aqueous cleans, and drying on tight-pitch trench patterning. As the trench etch and aqueous cleans typically makes the surfaces of the ILD hydrophilic, the drying step can generate sufficient hydrodynamic (capillary) force to overcome the mechanical strength of the ILD and pull opposing lines of ILD together into a "zipper" structure.[25] Figure 1(c) shows a top-down SEM image after trench etch where the compressive stress of the upper hardmask is able to overcome the restoring mechanical force of the ILD and bend patterned lines into wiggling "S-curves."[18,26–28] Figure 1(d) is a cross-sectional transmission electron microscope (TEM) image showing penetration of the barrier metal into the porous ILD during deposition,[29,30] which could present a reliability risk due to metal diffusion.[31] Due to these challenges, some companies are moving toward the integration of lower porosity materials. Successful implementation of highly porous materials will require both novel integration and proper material design. After a brief description of some of the proposed methods for the integration of highly porous ILD materials, the rest of this paper will focus solely on the materials challenge associated with generating a highly porous material with optimal properties.

Academic and industrial researchers have proposed clever solutions to the integration of porous low-k materials by making certain regions of the ILD nonporous. Initially, it was proposed to integrate the as-deposited nonporous composite of backbone and porogen species through metallization and to remove the porogen species at a later stage.[32] While the nonporous composite film minimized diffusion of reactive etch gases during etch or metal species during deposition, film shrinkage during final porogen removal led to reliability issues. As proposed by IBM, the post porosity plasma protection ("P4") scheme involves temporarily infusing a fully cured porous ILD with a second pore-filling material that can be removed without damage to, or shrinkage of, the backbone network.[7,33,34] Another option for etch protection is to use a sufficiently low temperature etch such that nonreactive etch gases spontaneously diffuse into and reside within the porous network of the bulk material.[35] The condensed gases then prevent the diffusion of highly reactive species during etch and therefore minimize backbone damage in a method similar to P4. The difference is, however,

https://doi.org/10.1557/jmr.2015.313 Published online by Cambridge University Press

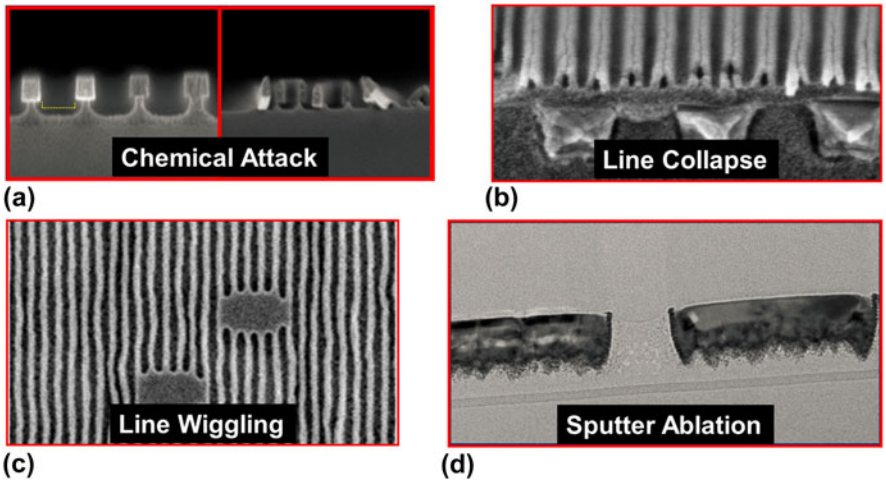


FIG. 1. Examples of integration challenges using porous ILD materials: (a) cross-sectional SEM image of CD blow out during cleans; (b) tilt SEM image of line collapse during cleans; (c) top-down SEM image of line wiggling after trench etch, and (d) cross-section TEM image of metal penetration into the underlying ILD during deposition.

that when the film warms up to room temperature, the condensed gases cleanly boil off to regenerate the porous network. A different scheme to prevent diffusion during metal deposition is to make the top surface of the ILD nonporous through either the deliberate addition of new material,[36,37] called pore sealing, or through surface densification by plasmas.[38,39] As opposed to the P4 process, the sealing layers remain in the structure and can increase the total effective capacitance. A more detailed discussion of pore sealing can be found in the review by Maex et al., and the references within.[6]

While the processes described above can provide temporary strength to low-*k* ILDs during integration, porous ILD materials will ultimately need to be strong enough to survive subsequent chemical treatments as well as mechanical stresses such as chemical mechanical polish (CMP)[30] and packaging stresses[40] at end of line. To this end, designing chemically stable, highly porous, mechanically robust ILD materials is critical to ensuring success of capacitance reduction schemes. This has been a difficult challenge for the industry as it has often been possible to deliver 2 but not all 3 of these critical parameters in one ILD material. In the Components Research Division of Intel Corporation, we have designed a porogen-backbone system we call TITAN that provides improvement on all three of these critical parameters through careful design of the backbone and porogen precursors. In hopes to spur more research and development on low-*k* films, we share some concepts we found critical to the development of porous low-*k* films.

II. DEPOSITION AND MOLECULAR DESIGN OF HIGHLY POROUS DIELECTRIC MATERIALS

Industrial dielectric thin film materials are deposited primarily using two methods: plasma-enhanced chemical vapor deposition (PECVD) and spin-on. Much of the early work on porous low-*k* films was performed by chemical suppliers (e.g., Shipley, JSR, Rohm and Hass, Dow and others) using the spin-on technique. Due to the challenges associated with inserting new materials into integration processes optimized on other materials, early spin-on films suffered from extreme chemical and mechanical damage.[41] It wasn't long, therefore, before PECVD films showed significant results and industrial interest. Over the past decade and a half, there has been a lot of successful research into the chemical mechanisms underlying the structure–property relations of porous materials, and the result is that both spin-on and PECVD materials are currently showing significantly improved properties. The review articles by Volksen et al.,[4] Maex et al.,[6] and the references therein provide excellent background on material development and integration challenges of these materials. Below, we will briefly summarize the critical processing steps needed to make highly porous films, with a larger focus on the spin-on technique because TITAN is a spin-on film.

Figure 2 shows a typical scheme for the fabrication of highly porous materials involving molecular units that will make up the backbone network of the final film (green dots) and molecular units that are volume placeholders (white dots) often referred to as "porogens." By adding more porogen into the film, the resulting porosity is expected to be increased.[42] For spin-on films, the first step is to create a stable liquid solution consisting of solvent, backbone, and porogen species, the latter of which are typically large molecules or polymeric oligomers.[43] The solution is then deposited on a wafer by spin coating and a randomly organized solid mixture [Fig. 2(a)] is expected after solvent removal bake. The next step in the process is to apply a stimulus (e.g., heat, light, etc.) that will cause the backbone (and possibly also

https://doi.org/10.1557/jmr.2015.313 Published online by Cambridge University Press

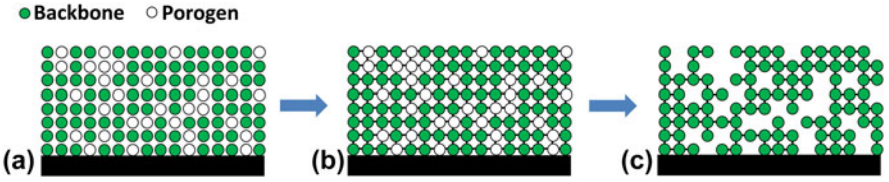


FIG. 2. A graphical description of (a) the porogen and backbone mixture that is coated on a wafer, (b) the resulting network after the backbone species have crosslinked via covalent bonds, and (c) the resulting network after the porogen molecules have been selectively removed.

the porogen) species to crosslink into a solid network [Figs. 2(b)].[44,45] For spin-on materials, this process is typically a mild thermal bake at 100–300 °C for a few minutes and is therefore referred to as a "soft bake." The amount of crosslinking can be inferred by the amount of thickness loss after solvent rinses. Films deposited using a PECVD technique[9,46] are formed from highly reactive gas-phase free-radicals that can couple into a cross-linked covalent bond network as deposited [Fig. 2(b)].

The final step in the formation of PECVD or spin-on porous films includes removal of the porogen species [Fig. 2(c)], which can be performed through thermal decomposition,[43] selective plasma etch process,[47] or solvent extraction.[48,49] The resulting film is a porous network of backbone species, may contain porogen residues,[50–52] and may be subsequently cured by treatment with UV, e-beam, or other film hardening processes.[53–59] Spin-on materials typically undergo porogen removal through a "hard bake" thermal degradation step at temperatures in the range of 350–450 °C for a few minutes followed by a UV or e-beam cure process for hardening. PECVD materials often go directly from deposition to e-beam or UV cure process for simultaneous removal of porogen and backbone hardening, but these steps can be separated.

To work successfully within the spin-on deposition technique, several critical chemical properties had to be designed into the TITAN backbone precursor. The first three key properties are high molecular weight (MW ≳ 500 Da), a high number of thermally activated functional groups for cross-linking, and following network formation, inherent thermal stability at 400–450 °C. The high molecular weight is needed to prevent volatilization during soft bake conditions.[60] The thermally activated groups also need careful consideration: they should not be so reactive that they crosslink at a non-negligible rate at room temperature, which can lead to precipitation during shelf storage.[45] But these groups need to be reactive enough such that the controlled crosslinking reactions can occur below or near the glass transition temperature (T_g) of the solid mixture of Fig. 2(a). If a crosslinking reaction requires a temperature higher than T_g, then the solid mixture of Fig. 2(a) may evolve into a mobile state which can lead to material agglomeration (thickness roughness) and backbone/porogen phase separation.

The porogen species also require careful chemical control. Typically they are hydrocarbon materials that can be selectively removed either completely or incompletely to leave behind porogen residue species by thermal decomposition at 400 °C. For spin-on materials, the porogen species will need to be of similar polarity as, and/or possibly reactive with, the backbone precursor to be soluble in the same solvent and to not phase segregate into large irregularly placed "killer pores" during soft bake.[44,61,62] Such killer pores have radii in the 20–50 nm size range, are clearly observable by cross-section SEM, and represent excursions in an otherwise tightly controlled and much smaller pore size distribution. We have observed both solubility and killer pore size challenges when the backbone and porogen polarity values are not properly tuned. Further information on the chemical optimization of porogen species can be found in the review articles of Volksen et al.,[4] and the reference therein.

The backbone molecular species for TITAN and other related films were created through chemical synthesis in our materials chemistry lab. We have found that the number of highly reactive groups on a backbone oligomer is critical to achieve high porosities. Conceptually, in order for the network of Fig. 2(c) to be able to retain its shape, the backbone molecular units need to be rigid enough to preserve bond angles and must have the ability to bond to multiple neighbors (up to 4 is shown in Fig. 2). It is clear that a backbone molecular unit that can only bond to two neighbors won't be able to form a highly cross-linked network.

We designed four backbone oligomer molecules with different integer numbers, n, of reactive groups. Each oligomer was separately mixed with different amounts of porogen, deposited on wafers, soft baked at 200 °C for 5 min, hard baked at 400 °C for 10 min, measured on a variable angle spectroscopic ellipsometer (VASE), and fit to Cauchy models with good mean square error values. The refractive index (RI) values, which can be used to monitor porosity,[63,64] at an optical wave length of 637 nm are presented in Fig. 3. Without the addition of porogen ($x = 0$), all films were non-porous with refractive indices between 1.48 and 1.52. This variation in RI is likely due to slight film compositional changes as a result of adjusting the relative amounts of reactive

https://doi.org/10.1557/jmr.2015.313 Published online by Cambridge University Press

versus non-reactive functional groups. With increased mass loading of porogen, the different precursors resulted in different final RI, and hence porosity, values after hard bake. For $n = n$ (Fig. 3, red squares), no porosity was observed due to the RI always being greater than 1.48. In this case the number of reactive groups was too small for the cross-linked network to maintain its shape and the network collapsed (i.e., lost thickness) upon porogen burn out. The increase in RI at high porogen loadings is expected to be due to the increased amount of porogen residues at high loading fractions. As the number of reactive groups per backbone molecule is increased (e.g., from $n = 2n$, to $2.5n$, to $5n$), the resulting films exhibit increasingly lower film shrinkage and increasingly lower RI values with increased porogen loading. The TITAN film, which contains $5n$ reactive groups per backbone molecule (Fig. 3, green circles), showed the lowest film RI values, and was the focus of further study.

While the data presented here clearly demonstrate the importance of the number of backbone reactive groups in establishing a strong porous network, similar trends in porosity versus collapse have been observed for PECVD films made from the same backbone precursor but with different porogen species.[42] The model of Fig. 2 is therefore simplistic in that the chemical distinction between backbone and porogen will start to blur; the film is not well approximated by distinct circles of unique color. Consistently, PECVD films have been shown to exhibit chemical scrambling between porogen and backbone precursors during deposition and cure, and the resulting film network may not correlate with the properties of the individual components.[65] While the relatively lower chemical energy available during spin-on processes (i.e., no plasma) would suggest relatively smaller chemical interaction during deposition, backbone-porogen interactions could still occur during baking steps. Specifically, porogen molecules may decompose into volatile species and/or partially into fragments that connect backbone unit that might not have otherwise formed. In such cases, the chemical interactions between backbone and porogen species can play a role in the final network structure, strength, and porosity; understanding these interactions is an important part of material design.

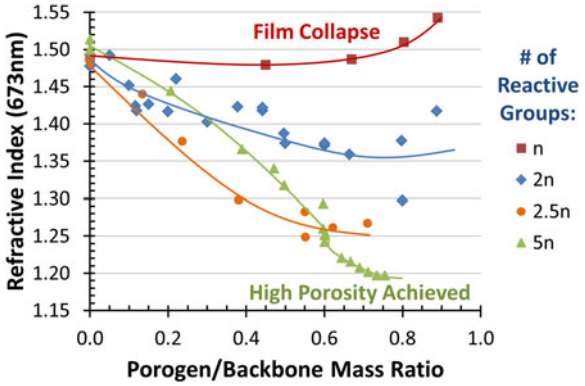


FIG. 3. RI values after hard bake for films made from Intel-synthesized backbone molecules containing various numbers of thermally active reactive groups mixed with various amounts of porogen. Solid lines are guides for the eye and do not represent fits to the data to any functional form. The reason for the differing trends in RI versus porogen loading for various n is currently unknown, but could stem from different yields of porogen residue incorporation versus n and/or different packing geometries of porogen and backbone versus porogen loading and n.

The set of TITAN films of various porogen loading was cured at 400 °C or greater under broadband UV illumination using a conventional tool for 1 min.[53,66,67] This process improved the mechanical strength and made the films more hydrophobic, but only mildly changed RI, porosity, and pore size distribution, which were measured using standard ellipsometric porosimetry (EP).[9,63,68,69] EP results from toluene and 2-propanol were nominally identical with errors in the 1% volume range and the data are shown in Fig. 4. The dielectric constant, k, values of the TITAN films were measured on a Hg probe with calibrated area of 0.022 ± 0.01 cm^2 at a measurement frequency of 100 kHz under accumulation voltage conditions. Also shown in Fig. 4 are other PECVD ILD films (The ILD0, ILD1, ILD2, and ILD3 PECVD films in this work are merely meant to represent the range of properties attainable with this deposition technique and are not meant to represent industry standard or state-of-the-art values. Their results are included because they could be measured on the exact same toolsets under the exact same conditions as the TITAN film; they are therefore meant as a general reference and not as a basis for fundamental chemical or structural comparison.) and two forms of the Maxwell Garnett approximation [Eq. (4)]: the solid black line (MG Fit 1) was obtained by assuming spherical voids of vacuum ($k_1 = 1$) in a bulk matrix of TITAN ILD ($k_0 = 3.4$); the broken black line (MG Fit 2) was obtained by assuming spherical inclusions

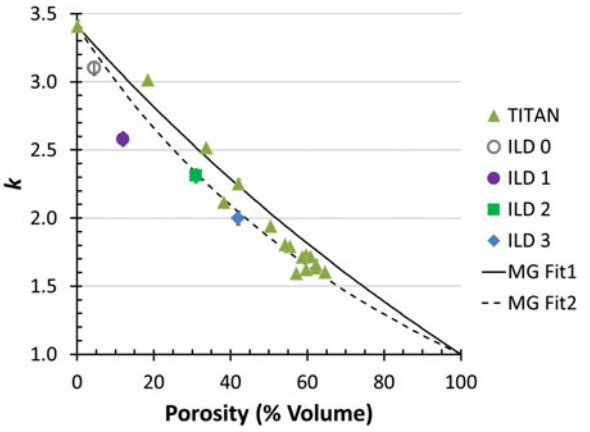


FIG. 4. Dielectric constant, k, values for the porous TITAN and other PECVD films relative to the Maxwell Garnett models as a function of their pore volume.

https://doi.org/10.1557/jmr.2015.313 Published online by Cambridge University Press

of TITAN ILD (k_1 = 3.4) residing in vacuum (k_0 = 1.0). Taken together, the two MG cases are expected to bound the real structure of the ILD as it transitions from low porosity (better fit by MG Fit 1) to high porosity (better fit by MG Fit 2). Due to the high number of reactive groups on the backbone molecules, n, the TITAN film can achieve porosities as high as 60% and k-values consistent with the Maxwell Garnett approximation as low as 1.60.

III. CHEMICAL STABILITY OF DIELECTRIC THIN FILMS

Films of porosity greater than 30% are generally assumed to have a completely interconnected pore network as predicted by percolation theory.[12–15] This presents a serious challenge to integration from a diffusion perspective: etch and cleans chemicals can permeate and chemically react with, aka "damage," the network; downstream atomic layer deposition (ALD), CVD, and/or PECVD deposition can result in the infiltration of metals into dielectrics, which could be bad for electrical leakage, capacitance, and/or reliability reasons. Of particular concern are dry etch processes not only because the etch plasma is specifically designed to react and volatilize the backbone species but also because plasma processes tend to eliminate pendant Si–CH_3 groups needed for hydrophobicity.[22,70] The chemically damaged areas of the bulk porous material tend to absorb moisture,[69,71] become attacked by wet cleans,[23,72,73] and result in mechanical, leakage, capacitive, and/or reliability risks.[74,75]

While the implementation of either cryogenic etch,[35] post porosity plasma protection,[7,33,34] and/or the pore sealing process[36–39] can help, there may be other processing steps in the integrated flow where the infiltration of plasma or liquid chemical into porous ILD is unavoidable. It is therefore desired to have the porous backbone be as chemically robust as possible to both plasmas and wet chemical solutions of acids, bases, and/or peroxide solutions. There are generally two approaches toward designing robustness against these types of chemicals. The first method is to prevent the reactive species from getting inside the porous film in the first place; the second method is to make the backbone material inherently stable to the aggressive chemical. For plasma processing steps, minimization of diffusion can be accomplished through either densification of the surface during etch, and/or controlling the tortuosity of the interconnected pore structure. In the first case, densification usually results in a degradation of the dielectric constant and the layer may be subsequently dissolved during cleans.[72,76] For the second case, the depth of damage layer induced by the plasma is a complicated trade-off between diffusion, recombination and reaction.[21,77] Not only is tortuosity difficult to control for various porosities,[78] but it will likely also reduce the mechanical strength of the film due to the formation of moments during mechanical loading (vida infra). Designing the backbone to be more inherently stable toward the specific plasma species is therefore important. Modeling has shown that the oxygen plasma stability of Si–R–Si groups, such as those implemented into TITAN precursor, is higher than for Si–CH_3 groups.[79]

Prevention of chemical diffusion of aqueous wet chemicals is more straightforward: hydrophobic termination of the pore walls will prevent aqueous solutions from wicking into the pores due to surface tension reasons.[68,73] Hydrophobic pore surface character and plasma stability is achieved by introducing thermally stable carbon-containing groups into the final network by using precursor with similar functionalities, e.g., 3MS, DEMS, TMCTS, DMDMOS, BTE, and others.[4,60,70,80–83] The carbon-containing groups can either exist at a terminal position [e.g., Si–CH_3, Fig. 5(a1)] or internal network position [e.g., Si–R–Si of Fig. 5(b1), where R = CH_2, C_2H_4, C_6H_4, or etc.]. There are times when the amount of carbon in the film is not sufficient to repel aqueous chemicals; this can either happen because of insufficient carbon as deposited, carbon loss from processing damage has occurred, or because surfactants in the chemicals are used.[70,80,84] In these cases, proper chemical design of the backbone can improve wet etch rates despite a hydrophilic inner pore surface structure. For example, when the cleans chemicals come close to the film network, a nucleophile (e.g., a dissolved species of $^-$OH, F^-, HF_2^-, etc.) might attack a silicon atom near a pore surface [Figs. 5(a1) or 5(b1)] to form a pentavalent transition state (a2 or b2).[85] Since the Si–O^- species is a weaker base than any of the nucleophiles listed above, a subsurface Si–O–Si bond can be favorably broken (a3). Upon attack of the same silicon atom by two more nucleophiles, the species can be removed (etched) from the surface (a4). Since the conjugate bases of most alkyl groups are stronger than the nucleophiles listed above, breaking a Si–R–Si backbond to form Si–R^- will not be favorable.

Periodic mesoporous organosilicate (PMO) materials containing Si–CH_2–Si groups have demonstrated enhanced stability to aqueous alkaline base solutions.[84] Similarly, the Si–R–Si type of carbon existing within 50% porous TITAN provides enhanced stability over the Si–CH_3 termination on the Si–O–Si framework of the 30% porous PECVD ILD 2 film. Both forms of carbon are acceptable in terms of ensuring stability against aqueous HF for the unprocessed films (Fig. 6 solid lines with filled symbols). Both films were then subjected to a CH_xF_y plasma dry etch for the same length of time and both lost 40 nm of film thickness. While Fourier transform infrared (FTIR) analysis showed less fractional loss in the Si–R–Si mode of the TITAN film relative to that lost by the Si–CH_3 mode of ILD 2 (data not shown), both films exhibited surface and pore surface wall damage as exemplified by low water contact angles

https://doi.org/10.1557/jmr.2015.313 Published online by Cambridge University Press

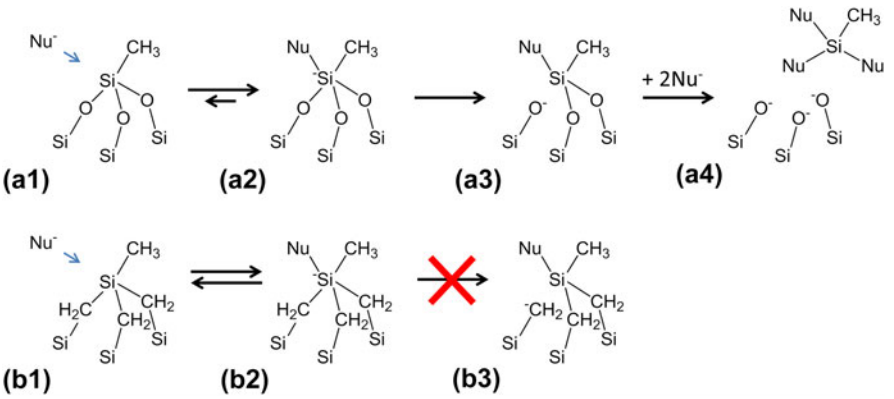


FIG. 5. Chemical structures showing the attack of a nucleophile (Nu^-) on the silicon atom of an ILD network (a1 and b1) to form an intermediate species involving a pentavalent coordination state of the Si (a2 and b2). In both cases, the pentavalent species could evolve to release the nucleophile again (a1 and b1). If the Si atom has Si–O–Si backbonds, the pentavalent species could also evolve to break a Si–O–Si backbond to form a terminal $Si–O^-$ site (a3); if this happens two more times, then the surficial silicon atom can be removed (etched) from the surface (a4). Since alkyl bases are stronger than most nucleophiles considered here, the Si atoms with Si–R–Si backbonds (here R = CH_2) would not be broken, the structure shown in (b3) would not form, and (b2) would return eventually back to (b1).

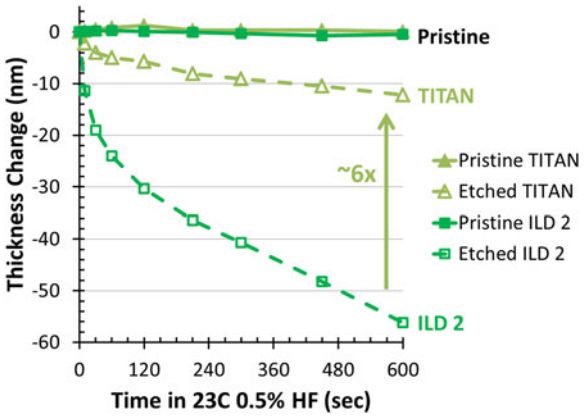


FIG. 6. ILD film thickness change versus time in aqueous 0.5% HF for pristine 50% porous TITAN (solid light olive green), 30% porous PECVD ILD 2 (solid dark green), and those same films after 40 nm etch in a CF_xH_y plasma (dashed lines and open symbols of similar color). Non-patterned film thickness values were measured by variable angle spectroscopic ellipsometry.

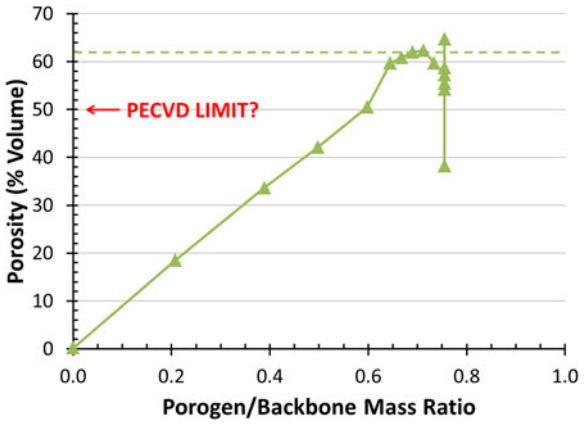


FIG. 7. Film porosity versus percent mass loading of porogen for the TITAN film. Note that the film porosity becomes more unstable and does not go higher than 62% despite the addition of more porogen mass fraction.

and water vapor uptake values from EP equal to the film porosity.[71] It was therefore assumed that an aqueous HF solution would rapidly permeate the entire porous networks of both films. Figure 6 shows the significantly higher HF stability (post-etch) imparted by the remaining internal Si–R–Si network of TITAN relative to the Si–O–Si network of ILD 2 (Fig. 6, dashed lines with open symbols).

IV. LIMITS ON POROSITY

As researchers strive to continually reduce *k*-value, materials with increasingly higher porosity are targeted. But are there practical limits to material porosity? TITAN films, like many other in the industry,[86] cannot be made with arbitrarily high porosity. Figure 7 shows the porosity of TITAN films as a function of the amount of porogen added to the spin-casting solution. At low porogen weight fractions, the resulting film porosity follows an expected linear trend. Above 60 wt% of porogen, the film no longer continues to increase in porosity and reaches a maximum porosity around 62% volume; note that at 75 wt% porogen the porosity becomes relatively unstable. Similar trends have been presented in the literature,[86,87] but few reports actually show the instability and/or film collapse (porosity decrease) upon thermal cure of very high porogen loadings. Our experience suggests a limiting maximum porosity near 50% volume for PECVD films using conventional tooling, but this has not been rigorously explored.

Understanding the fundamental limitations on porosity is important. One model to explain the limiting maximum porosity is percolation theory,[14,88] which is described graphically in two dimensions in Fig. 8. A fully

https://doi.org/10.1557/jmr.2015.313 Published online by Cambridge University Press

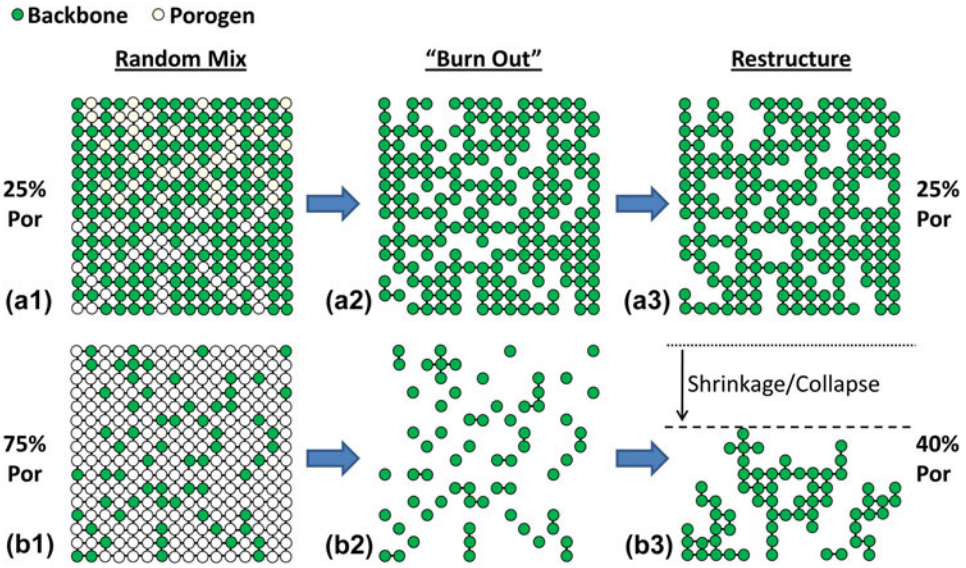


FIG. 8. Graphical representation of networks of backbone and porogen species at 25% porogen loading (a1, a2, a3) and 75% porogen load (b1, b2, b3) after film crosslinking (a1, b1), porogen removal (a2, b2), and film restructuring (a3, b3).

cross-linked square grid network containing 0.25 site occupancy of randomly placed porogen molecules (which is the same as 25% porosity or a backbone site occupancy of 0.75) is shown in Fig. 8(a1); a key requirement of percolation threshold (PT) is random placement. Upon removal of the porogen by simulated "burn out," the backbone molecules have not changed in placement due to the assumed rigidity of the backbone bond angles [Fig. 8(a2)]. Figure 8(a3) represents some structural rearrangement that could occur during curing steps, and both networks in Figs. 8(a2) and 8(a3) pass the PT since there is a continuous path of bonds from one edge of the film to the other. The PT for a 2D 4-coordinate square lattice corresponds to a backbone site occupancy of 0.59; below this an interconnected infinitely large network of backbone molecules would not exist. The 75% porogen content (backbone site occupancy of 0.25) of Fig. 8(b) clearly is below PT. Even if all backbone molecules of Fig. 8(b2) could be incorporated into a network, e.g., by allowing them to fall downward and bond with the nearest possible backbone site, the resulting network [Fig. 8(b3)] would contain only 40% porosity. While this represents an extreme case, it suggests how film collapse can lead to lower than expected porosity values.

While the structures of Fig. 8 represent 2D lattices, Table I gives site PT values and the corresponding maximum porosity values for three dimensional lattices having different coordination numbers.[88] For example, a 3D network composed of 4-coordinate tetrahedrally bonded units arranged in a diamond lattice could support a maximum porosity of 57%. If the backbone molecular units could bond to more neighbors (i.e., have a higher coordination), then a higher maximum porosity would be possible.

TABLE I. Table of maximum expected porosity versus site coordination number for a three dimensional randomly porous network. Adapted from Zallen.[88]

Lattice	Coordination	PT (site)	Max porosity (%)
fcc	12	0.20	80
bcc	8	0.25	75
rcp	<8	0.27	73
Cubic	6	0.31	69
Diamond	4	0.43	57

While this model is powerful, there are a number of real world complications that limit its direct applicability. First, few dielectric materials can be well represented by molecular units perfectly organized onto a periodic grid.[88] While a direct comparison of ordered and random networks is not trivial, the jammed random-close packed (rcp, CN $\sim$ 8) network results in only a slightly lower maximum porosity value relative to the body centered cubic (bcc, CN = 8) network. It is assumed, however, that as the density of the random network is reduced below the jammed matter limit the average coordination number will decrease, the site PT will increase, and the maximum porosity of that network will correspondingly decrease. Many silica-based dielectric films are composed of randomly interconnected corner sharing tetrahedral of silica (SiO_4) units.[85,88] Figure 9(a) shows one of these tetrahedra, and for amorphous dense glass each oxygen atom is the corner bridge to another tetrahedron through a Si–O–Si bond. PECVD and spin-on glasses made from these tetrahedral silica units are expected to have a 4 coordinate random lattice,[85,88] which by comparison with rcp/bcc trend may only have a slightly reduced maximum porosity relative to the diamond lattice.

https://doi.org/10.1557/jmr.2015.313 Published online by Cambridge University Press

The second complication is that neighboring backbone species may not always be connected via covalent bonds because condensation reactions for silica sols are known to require process control.[45,85,89] The networks of Fig. 8 graphically depict 100% probability of connection between sites with black lines. In sol–gel films, there may be neighboring Si sites that exist in the chemical form of the non-bonded [≡Si–OH + HO–Si≡] structure rather than directly bonded [≡Si–O–Si≡] structure (the symbol "≡" represents the three other bonds that silicon atom makes to the surrounding network). This adds a bond percolation component to what is being described as a site percolation network, and it is assumed that a reduced bond probability between neighboring backbone sites will increase the required backbone site occupancy for PT and decrease the maximum porosity of the network. For PECVD films, increases in deposition temperature[90] or higher subsequent annealing temperatures[91] seemingly improved the connectivity of the Si–O–Si bond network prior to porogen removal, which led to less shrinkage, lower *k*-value, and higher porosities. Similar optimization of the Si–O–Si network crosslinking prior to porogen removal has also been shown to be important for spin-on materials.[45] Bond percolation of networks containing silica tetrahedra will be similarly reduced for films containing Si–CH_3 groups. Cured films comprising a mix of SiO_4 and O_3Si–CH_3 tetrahedra are expected to have a coordination number between 3 and 4 and an overall maximum porosity below 57%.

The third complication is that the porogen placement in the network during deposition may not be considered truly random even if not deliberately controlled. Due to the high reactivity of free-radical species generated during PECVD deposition, such networks are expected to be better characterized as randomly mixed networks relative to spin-on films, which could have tethered backbone-porogen species and/or involve phase separation. Finally, aerogels and xerogels are not discussed in this context as they have complex structure forming and solvent removal requirements that are not applicable to percolation theory or to current industry standard ILD processing.[85,92]

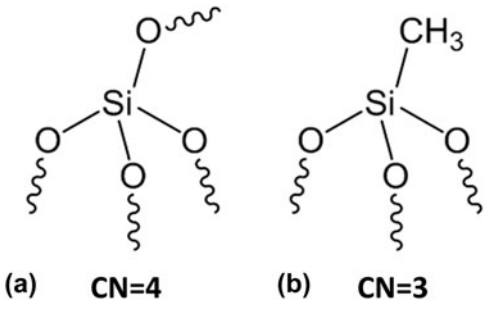


FIG. 9. A description of some typical connectivity units within a general CDO ILD: (a) a four-coordinate tetrahedral SiO_4 unit and (b) a three-coordinate tetrahedral O_3SiCH_3 unit.

Baklanov et al.[93] present films with unusually high porosity values (up to 80%), but as little structural information is given some of those films could be aerogels.

In contrast to terminal Si–CH_3 groups, internal Si–R–Si linkages can provide similar or better chemical stability without reducing the bond coordination number of the attached Si atom (and therefore without compromising the mechanical strength[94]). As described in Sec. III, the TITAN film employs a significant number of Si–R–Si bonds, but that alone cannot explain why the maximum porosity of TITAN (62%) is greater than PT expected for 4-coordinate units. Instead, it is the high number of reactive groups per backbone molecule and its molecular structure that raises the maximum coordination number of a TITAN molecular unit to 6. Since we expect the TITAN film to be better described by a random lattice (rather that a cubic lattice), and since we expect the average backbone coordination to be somewhat less than the maximum possible of 6, the experimentally observed maximum porosity of 62% is reasonable given the maximum porosity of 69% for cubic lattices.

V. MECHANICAL STABILITY OF DIELECTRIC MATERIALS

Mechanical strength is a concern for highly porous materials. While the mechanical strength during several integration steps can be increased by temporarily making films non-porous via the P4 process (discussed above), porous films will ultimately need to be strong enough to survive CMP[30] and packaging stresses.[40] Mechanical strength has typically been ascribed to the amount of internal network crosslinking within a film.[86] The high number of reactive groups on a TITAN backbone molecule not only enables a high porosity, as shown above, but could also result in high mechanical strength. On top of this, the addition of certain carbon containing species[94] such as bridged oxycarbosilanes[95] into the backbone network have been shown to exhibit a mechanical benefit relative to more oxide-like SSQ films at

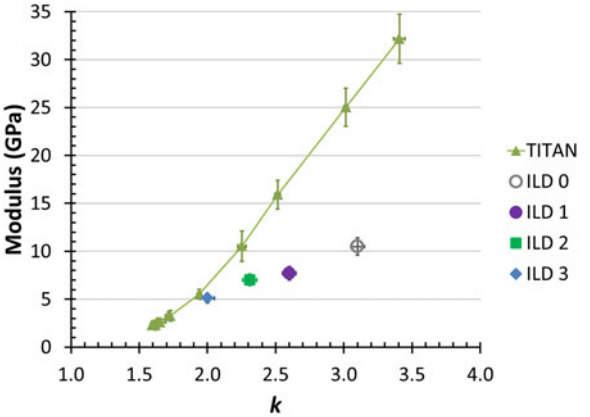


FIG. 10. Modulus from nano-indentation versus dielectric constant, *k*, for TITAN and various PECVD ILD films.

https://doi.org/10.1557/jmr.2015.313 Published online by Cambridge University Press

matched k-value. Figure 10 shows the Young's modulus values extracted for TITAN films as measured from continuous stiffness nano-indentation method using a Berkovich tip[96–99] relative to some other PECVD CDO films. The strength of TITAN is clearly apparent at lower porosities ($P < 43\%$ volume, $k > 2.2$) relative to the other CDO ILD films. Here, the mechanical strength is more determined by the backbone bond density rather than the pore structure. As mechanical strength tends to be limited by the weakest springs in a network, each component of the TITAN backbone molecular structure was designed for strength: rigid molecular structures were connected by inflexible linkers that are as short as possible. At higher porosities ($k < 2.2$), the strength of TITAN is reduced, but even the 50% porous ($k = 1.95$) version of TITAN still exhibits a 10% improvement in stiffness relative to the PECVD ILD 3 film, the latter of which required a significant effort in the optimization of mechanical strength. While the modulus at $k = 1.95$ is greater than or equal to many[47,59,61,91,96,98,100,101] but not all[45,102] reports in the literature, modulus values for lower k versions of TITAN rapidly decrease below conventionally acceptable levels.[30,40] At these high porosities, the mechanical properties become more and more dependent upon the pore structure,[96–99,103] and this will be discussed in more detail in the Sec. VI.

Similar to other films in the literature,[96,97,99] the TITAN film exhibited a linear decrease in cohesive energy, as probed by dual cantilever beam measurements, versus porosity with a slightly relaxed slope of −0.87 instead of −1 (data not shown). At matched porosity to ILD 2 (30%), the TITAN film exhibits a 28% increase in cohesive energy density. Historically, the adhesion of spin-on films to adjacent materials has been a challenge.[41] While we have not measured the adhesion energies of TITAN to relevant materials in a scientific way, the integration of 50% porous TITAN into metalized damascene structures of 160 nm pitch has not resulted in delamination through final CMP.

While TITAN shows a number of improvements over typical PECVD CDO ILD films, further capacitance scaling would require films with higher maximum porosities and higher mechanical strengths at such porosities. In the Sec. VI we will show how deliberately ordered structures can not only break beyond the porosity limitations imposed by PT on randomly ordered porous networks, but can also deliver mechanical improvements.

VI. BENEFITS OF ORDERED POROSITY

The maximum porosity values defined by percolation theory only apply for periodic networks where sites (or bonds) are removed at random. Figure 11 shows two graphical representations of a 75%-by-volume porogen-containing square grid network. The network on the left was created using a random number generator. The network on the right has the backbone units (green dots) organized into a pattern that is fully interconnected even after the porogen units (white dots) are removed.

An organized pore structure can therefore exceed the limits of PT. Examples of ordered films exhibiting porosity values near or greater than the 4-coordinate limit of 57% are PMOs,[84,104,105] jammed packed hollow spheres,[106] and metal-organic frameworks (MOFs).[107–110]

To further investigate the mechanical and porosity benefits that ordered structures can provide, we couple modeling and experimental results on films with ordered pore structures.

A. Finite element modeling technique

Several reports in the literature have simulated overall mechanical properties of porous ceramic materials through various homogenization approaches. Some of these models account for the topology of the pores through size parameters and can match experimental results over a wide range of porosity values reasonably well provided the parameters are calibrated properly. Often times different values of parameters work at different porosity ranges.[111,112] At high porosities, the interaction of connected pores and backbone load paths strongly influence the overall properties which necessitates an accurate computational modeling approach. In this work, a representative volume element (RVE) approach is adopted which conveniently lends itself to finite element (FE) modeling technique. A RVE is usually defined as the smallest block of a non-homogeneous material that captures the overall behavior of the heterogeneities and represents the mean macroscopic response.[113,114] Few other works have applied RVE-based FE modeling to porous films.[115] Here, different RVEs were generated by sampling experimental pore-size distributions and performing tensile tests to determine their overall moduli. Hexahedral elements of uniform size were used such that for a given total thickness, the element size corresponded to the size of a single TITAN or porogen molecule. Hence, removal of a single voxel element from the RVE for pore creation was structurally similar to removal of a porogen molecule. Typically 10 RVEs with 100 nm sides were generated and their moduli were averaged to estimate the modulus value at each porosity data point. Figure 12 shows examples of two generated RVEs with different pore shapes but with the same porosity and pore size distribution.

Figure 13 shows the experimental Young's modulus data for TITAN and other PECVD films (from Fig. 10) versus the porosity value of these films (from Fig. 4) along with the results from various FE modeling experiments. The FEM-generated modulus values for a given porosity were calculated relative to the non-porous case and were normalized to the experimental value of non-porous TITAN for comparison. Porous FE networks were

https://doi.org/10.1557/jmr.2015.313 Published online by Cambridge University Press

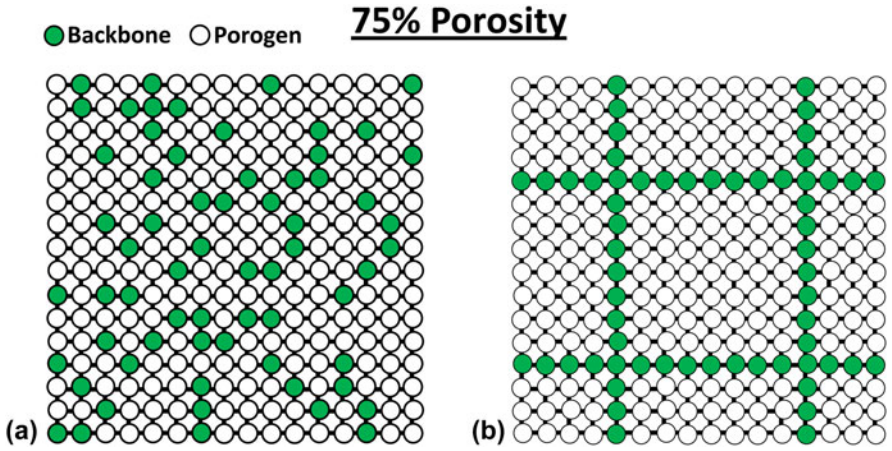


FIG. 11. Graphical depiction of a material composed of 75% porogen content with random porosity (a) and an ordered structure (b).

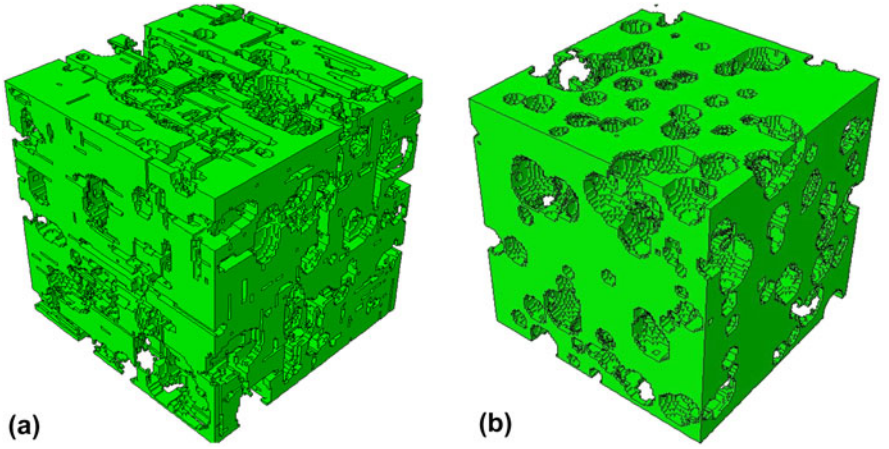


FIG. 12. RVEs with ellipsoidal (a) and spherical (b) pore geometries at ~53% porosity with pore sizes sampled from the experimental pore size distribution for TITAN (Fig. 14) at that porosity.

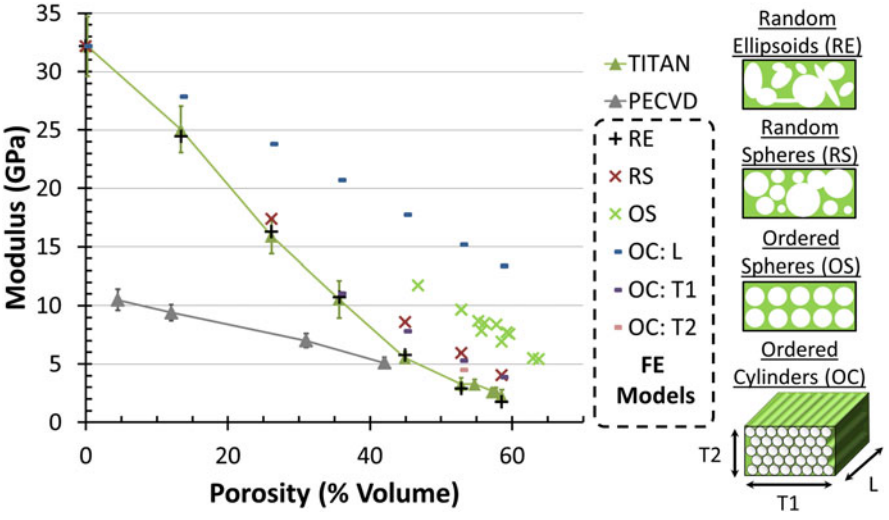


FIG. 13. Data and FE modeling of porous materials comparing films containing not-deliberately controlled pore structure to those with ordered structures.

https://doi.org/10.1557/jmr.2015.313 Published online by Cambridge University Press

generated by randomly placed pores of spherical [Fig. 13, red cross symbols; 3D image of 53% porosity shown in Fig. 12(b)] or ellipsoidal [Fig. 13, black cross symbols; 3D image of 53% porosity shown in Fig. 12(a)] pore shapes sampled from the experimental pore size distribution (Fig. 14) for TITAN at that porosity. (Note that, like many films in the industry,[9,86,116] the pore size of TITAN increases with porosity; this will be discussed further in Sec. VII.) Similar to other reports in the literature,[97,99] the experimental TITAN film data (Fig. 13, light green triangles) are best fit by the randomly placed ellipsoidal pores.

Experimental evidence for the existence of ellipsoidal pore shapes is given in Fig. 15 for the 45% porous TITAN film, which was infiltrated with a high atomic element (high Z) material deposited by ALD for TEM contrast. Some pores are circled in yellow broken lines to highlight the ellipsoidal structure. A sampling of multiple pores visible in the TEM sample resulted in a pore radius distribution with average equal to 3.4 nm and a standard deviation of 1.6 nm; this is similar to the pore size distribution given by EP, Fig 15(b).

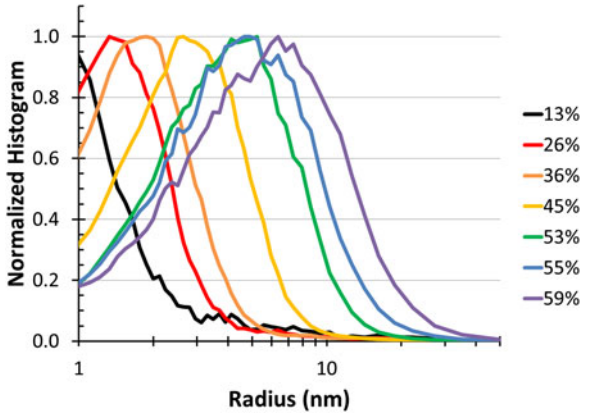


FIG. 14. Peak height normalized p size distributions obtained from EP adsorption isotherms for the TITAN film as a function of porosity.

FE models generated from randomly placed spherical pores of radius defined by the same pore size distribution (Fig. 13, red cross symbols) resulted in significantly higher modulus values. The reason for this relative increase in modulus can be understood by the FEM-generated stress contours resulting from a 1% strain in the vertical direction shown in Fig. 16 for 53% porous films. The film with ellipsoidal pores [Fig. 16(a)] results in stress contours that are more serpentine in nature and therefore have higher moments and correspondingly lower mechanical properties. In addition, there are large volumes of the backbone network (blue regions) that are not contributing to the load path. The 1% strain is therefore applied to only a small fraction of the film, which results in a lower average stress and therefore a lower overall modulus. In contrast, the network of randomly placed spherical pores with the same pore-size distribution [Fig. 16(b)] contains load path that are more straight and more uniformly distributed over the cross-section (i.e., fewer blue regions). A further improvement in mechanical strength comes from uniformly sized spherical pores place in an ordered array (Fig. 16(c), Fig. 13, green crosses) because the load is very evenly divided across the backbone network (very little blue regions) with load paths that are the most straight.

PMOs films are characterized by cylindrical pores of uniform radius that typically pack in a hexagonal close packed (hcp) pattern as described by the schematic at the top of Fig. 17. For this structure, the strongest axis is along the length of the cylindrical pores (Fig. 17, L; Fig. 13, blue dashes) because nominally all backbone material participates equally in the load transfer (uniform stress); the porosity scaling relationship with modulus is

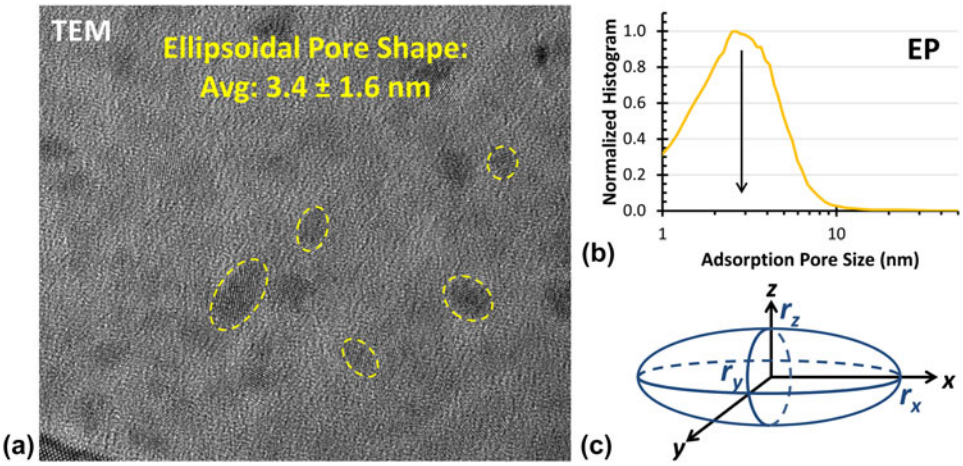


FIG. 15. TEM (a) and peak height normalized pore size distribution (b) obtained from EP of a 45% porous TITAN film infiltrated with proprietary ALD material of high atomic number used for imaging contrast. The pores appear to be ellipsoidal in shape, randomly placed, and oriented randomly relative to the long axis of the ellipsoid (c).

https://doi.org/10.1557/jmr.2015.313 Published online by Cambridge University Press

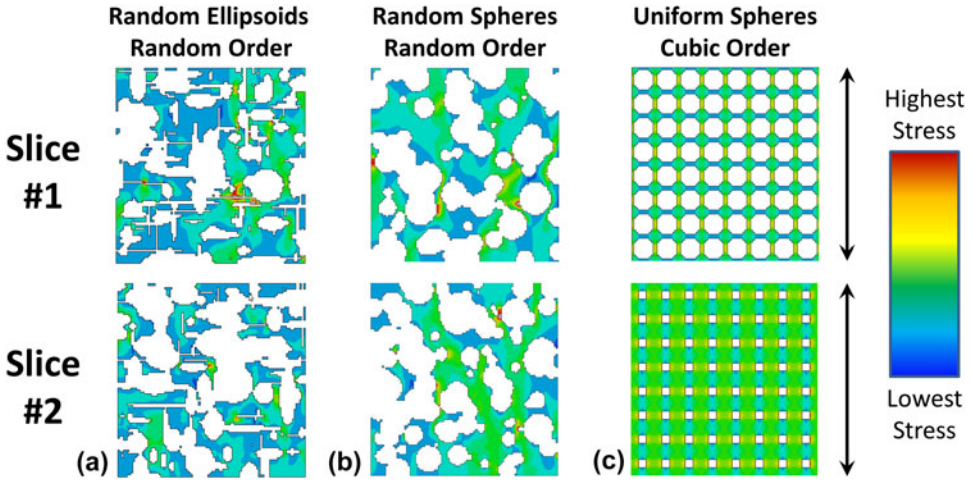


FIG. 16. FE Model of stress contours for cross-sectional slices of 53% porous materials that have different spheroidal pore structures: (a) randomly placed ellipsoidal pores showing the most convoluted 3D backbone network structure with areas of high stress (red regions); (b) randomly placed spheroidal pores following the same pore radius distribution but having fewer moments in the backbone loading path; (c) controlled placement of uniform 6 nm radius spheroidal pores in a cubic array.

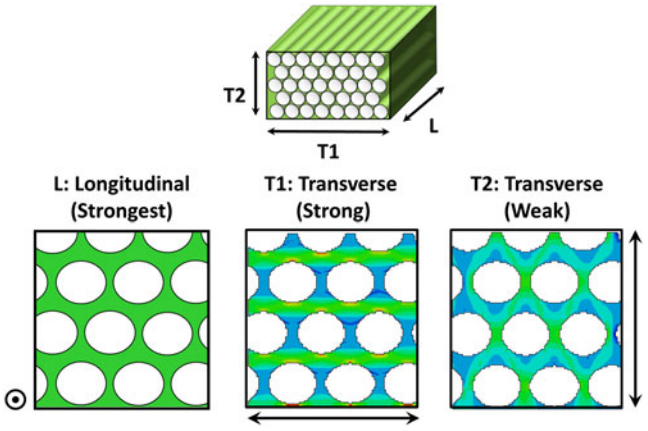


FIG. 17. Stress contours using the same color scale of Fig. 16 along different directions of strain for a structure composed of hexagonally packed horizontally aligned cylindrical pores with elliptical cross sections as described in the text: (L) strain applied out of the page such that all backbone material equally divides the load; (T1) strain applied left and right such that fewer material absorbs axial load; (T2) strain is applied up and down such that all load paths involve significant moments.

therefore linear. In the transverse directions, there is a stronger axis (Fig. 17, T1; Fig. 13, purple dashes) and a weaker axis (Fig. 17, T2; Fig. 13, pink dashes). As shown by the stress contour maps of Fig. 17, the T1 axis is stronger because the loading paths have more rectilinear character, while the T2 axis has loading paths with more moments.

B. Experimental PMO

PMO films allow for the generation of ordered mesoporous networks via self-assembly of the pore-forming surfactant and the backbone organosilica precursors.[48,49] Both the chemical flexibility of the backbone precursor and the ability to tune the pore size and porosity of the resulting ordered pore network make these materials of interest for low-*k* ILDs. The PMO of this work used backbone molecules that were similar in chemical composition and structure to the TITAN film and therefore exhibited no thickness change, similar to the TITAN film, in 0.5% aqueous HF for up to 10 min. Figure 18 shows EP isotherms for the TITAN and PMO films at 54% and 53% porosity values, respectively. Due to the surfactant and backbone self-assembly process of the PMO films, a much narrower pore size distribution (Fig. 18, inset) centered at a pore radius of 1.3 nm is observed relative to the wider pore size distribution centered at a radius of 2.5 nm for this TITAN film.

PMO materials were filled with the same high-Z ALD material for TEM image contrast, and Fig. 19 shows the highly ordered cylindrical pore structure: While the pores are clearly organized in a hcp pattern, the cross-sectional shape is better characterized by an ellipse with long axis parallel to the wafer plane. As this shape deformation has a mechanical impact due to an increase in the moment during vertical stress loading, the FE modeling of Fig. 17 and Fig. 20 used the experimental pore structure as inputs, which matches the experimental results for PMO films quite well.

Figure 21 shows that the ordered structure of a PMO can be maintained through trench patterning when using proper integration. Similar to other work,[117] this particular film was thicker and less well-ordered away from the air and substrate interfaces than the film in Fig. 19, but clear examples of ordered regions can be seen along the trench sidewalls and trench bottoms.

https://doi.org/10.1557/jmr.2015.313 Published online by Cambridge University Press

While the orientation of the pore direction for PMO materials deposited on flat surfaces currently cannot be controlled (domains of different direction are seen), deposition of these materials into features appears to have a guiding property. Figure 22 shows the self-arrangement of the PMO material along the axis of a trench within the trench when inside it and random orientation when above it. PMO materials could then work nicely in a sacrificial flow where the pore structure may be ordered by the topography of the patterned structure.

C. Metal-organic frameworks (MOFs)

MOFs[107,108] and metal-free covalent organic frameworks[110] are highly porous ordered structures and are starting to be considered as ILD materials in the back end.[109] We have chosen to make thin films of the ZIF-8 MOF to understand the benefits and challenges of applying this relatively new class of materials to dielectric applications. This particular MOF is made up of zinc atoms connected by organic imidazole molecules into an ordered 3D network. Synthesis of 50–500 nm thick films followed literature procedures.[118] Films made in this manner are crystalline, with lateral domain sizes greater than 100 nm and surface RMS roughness values obtained by AFM and SEM of around 9 nm [Fig. 23(a)]. VASE techniques did not produce good fits to Cauchy models as expected on the basis of the surface roughness. X-ray diffraction (XRD) spectra of the as-deposited films show a crystalline structure with results similar to that reported for other ZIF-8 thin films.[109] ZIF-8 films are claimed to have thermal stability[119] up to 450–500 °C but while the XRD spectrum of a ZIF-8 film after a 400 °C 30 min bake in N_2(g) only showed a slight decrease in peak intensities, SEM analysis [Fig. 23(b)] shows significant film cracking and thermal desorption spectroscopy indicates a loss of imidazole ligands among other species. While the bulk film may be thermally stable, surfaces and/or interfaces exhibit thermal instability.

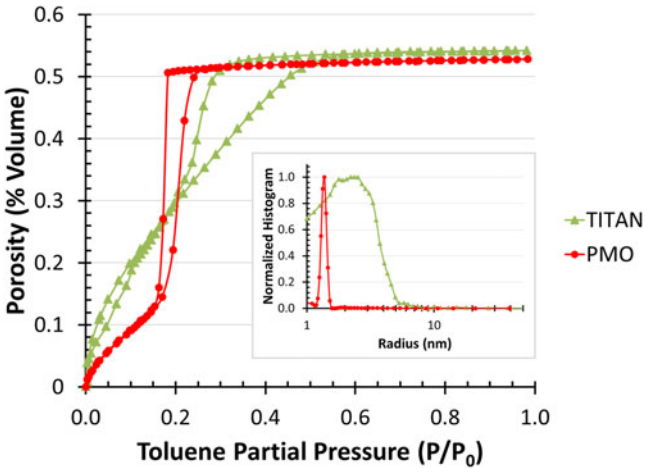


FIG. 18. Adsorption isotherm for both TITAN (green triangles) and PMO (red circles) showing 55 ± 1% porosity in the film for both cases. Inset: a much narrower pore size distribution is obtained for PMO relative to TITAN. The soft-bake, hard-bake, and curing of the TITAN film in this experiment was different from the films shown in Figs. 13–15.

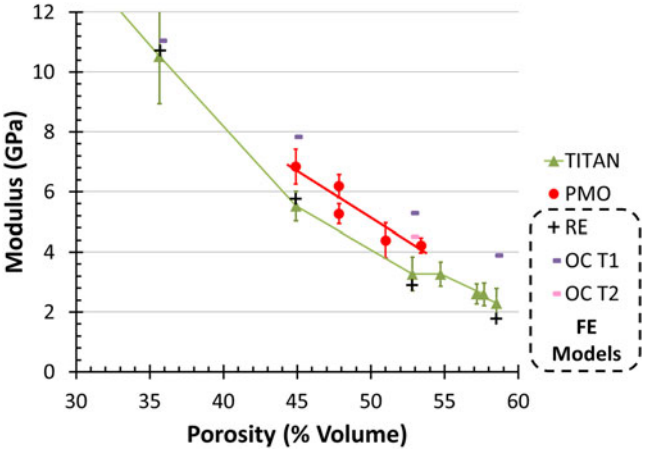


FIG. 20. Modulus versus porosity for TITAN, PMO T1, and PMO T2.

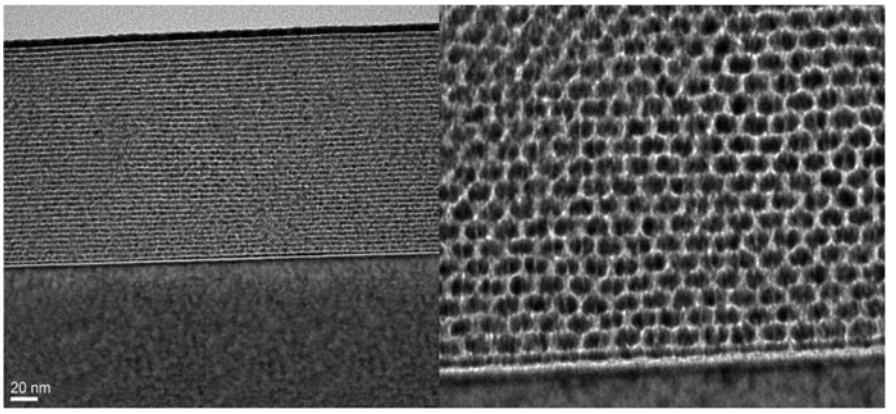


FIG. 19. TEMs of PMO film showing ellipsoidal cylinders aligned parallel to the substrate.

https://doi.org/10.1557/jmr.2015.313 Published online by Cambridge University Press

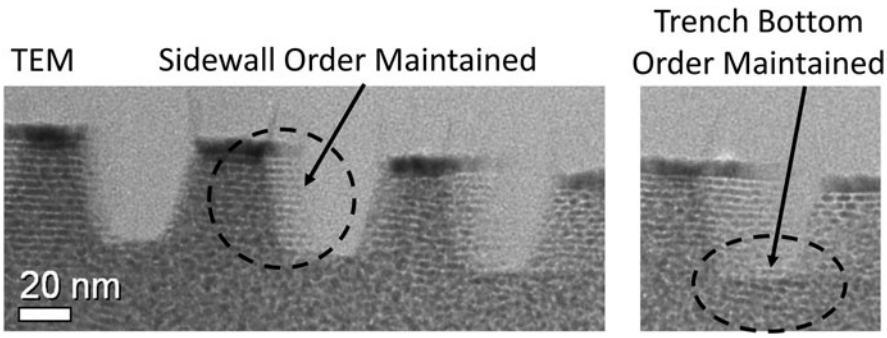


FIG. 21. TEM showing the ability of the PMO material to maintain their order when properly integrated through a trench etch.

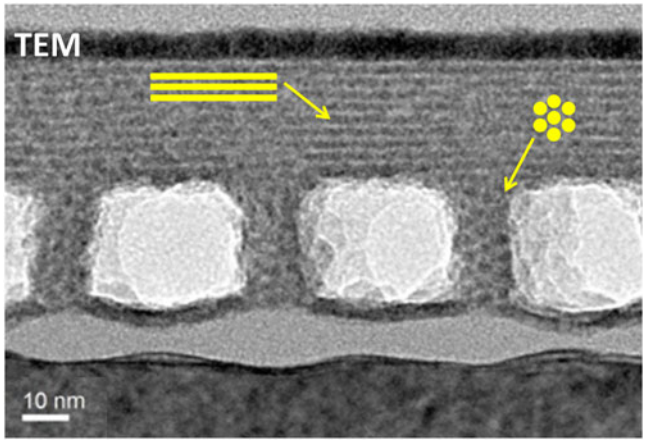


FIG. 22. TEM showing the ability of the PMO material to align within the guiding trench structure of the patterned substrate.

Molecular modeling predicts that ZIF-8 films have high (60% volume) porosity[119] with really low pore sizes (0.3 and 1 nm).[120,121] This presents a unique and desirable pore structure for ILD applications. MOF films were therefore measured using EP to probe the pore size and porosity values, which should show no absorption due to pore sizes smaller than the test molecules. Unlike other reports,[109] however, the toluene and isopropyl alcohol isotherms show irreversible behavior. The top-down and cross-sectional SEM images of Fig. 23(c) show significant film cracking after EP measurements. A ZIF-8 film immersed in toluene for 10 min showed film loss and recrystallization [Fig. 23(d)], consistent with the instability observed for these films during toluene EP measurements. While we are not sure if the particular method we used for the synthesis of ZIF-8 films resulted in the observed lower film thermal and chemical stability, future work on these materials should continue to monitor these concerns. As most of the film instability appears to be driven by grain boundaries, recent work demonstrating templated single-crystal growth[108,122,123] could result in significantly improved film properties.

As the ZIF-8 film is composed of zinc metal atoms bonded with aromatic hydrocarbon linkers, the dielectric constant and the electrical conductivity are concerns. ZIF-8 films of 100 nm thickness were deposited on highly conductive Si substrates (dopant density $> 10^{19}$ cm^{-3}). Dielectric constant values of 2.35 $\pm$ 0.2 were extracted from flat capacitance–voltage curves measured in air on a conventional mercury probe with a calibrated area using a 100 kHz sin wave of amplitude $\pm$0.1 V and a DC bias range of $\pm$1 V; the relatively large error in *k*-value stemmed from the thickness roughness observed on SEM but is within error of other reports for this film.[109] Electrical conductance (also called leakage) measurements between the range of $\pm$100 V were performed on the MOF films using the Hg probe (Fig. 24, red curves) or using a dedicated vacuum-capable probe for MOF samples with evaporated circular Al dots in air (Fig. 24, black curves) or under vacuum (Fig. 24, blue curves). For negative biases, the results measured on the Hg probe are relatively similar to the results measured in air using Al dots, but there is a larger variation between the two techniques for positive directions. The results from MOF samples with Al dots are similar to published results for metal-insulator-metal (MIM) capacitors.[109] Because the ZIF-8 films are known for gas[120,124] and solvent absorption[119] and because adsorbed gases can pose an electrical leakage risk, the electrical leakage was measured in vacuum to segment the inherent backbone leakage from possible gaseous inclusions. Samples were annealed for 12 h at 127 °C under vacuum (at 10^{-6} Torr) followed by 8 h of cool down to 27 °C and measured under vacuum (Fig. 24, blue curves). The dramatic reduction in leakage current ($>1000\times$ reduction at 2 MV/cm) for vacuum versus air measurements suggest that the backbone is not inherently leaky and that physisorbed gas species can play a major role in the leakage of these films under ambient conditions. At the moment we do not know which gaseous components of air or residual solvents could be contributing to the leakage current, but leakage measurements under controlled gaseous environments could segment the

https://doi.org/10.1557/jmr.2015.313 Published online by Cambridge University Press

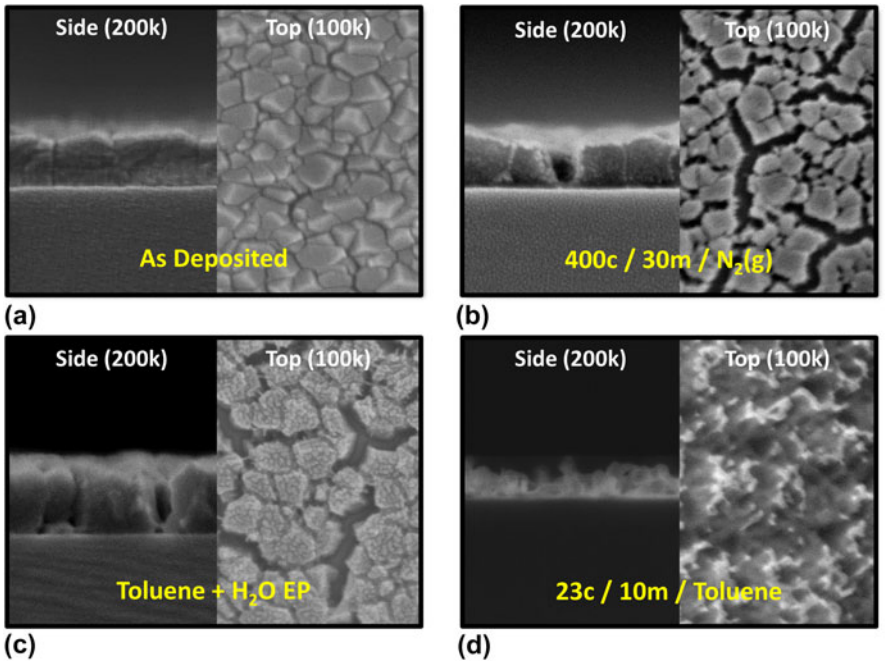


FIG. 23. Side and top-down SEMs for (a) a MOF film as-deposited after (b) a 30 min 400 °C thermal cure in nitrogen, or after (c) running a typical toluene EP experiment, or after (d) a 10 min immersion in 23 °C neat toluene. These images show the propensity of the film to crack or recrystallize.

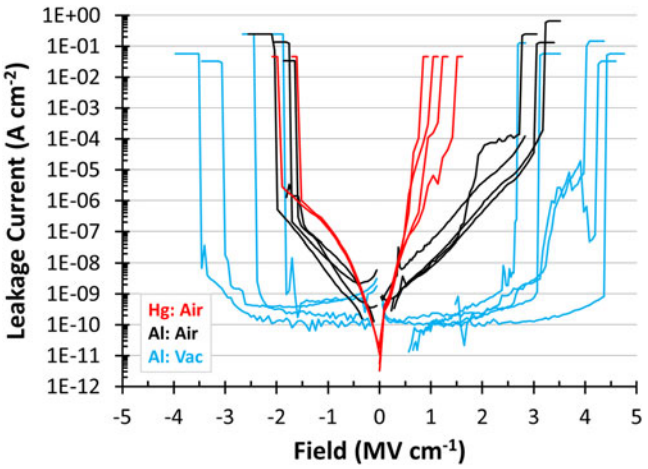


FIG. 24. Electrical leakage data on the ZIF-8 MOF film: (red and black lines) measurements performed in air, (blue lines) measurements performed in vacuum. The absorption of physisorbed water and/or other airborne species contribute a large amount to electrical leakage under air conditions, but the leakage of the metal-containing backbone is reasonable under vacuum for electric field values less than |2| MV/cm.

contributors. We notice that the leakage currents and breakdown fields exhibit quite a lot of variation; this could be due to incomplete annealing to remove all trapped gases/solvents from the film and/or variation due to breakdown along various grain boundaries. The single crystal growth methods for MOF films[108,122,123] measured under more controlled outgassing and vacuum conditions could show continued improvement in segmenting the leakage contributors. Future experiments and final integration of such materials, if possible, will clearly need to be done under conditions where electrically leaky gaseous components are avoided.

Table II compares some of the properties of the ZIF-8 MOF film relative to TITAN and one of the amorphous SiCOH films discussed above. The porosity and pore size distribution of the MOF could not be independently measured so the predicted values are cited.[16,120,121] The elastic modulus of 2.7 ± 0.2 was measured in the same way as for the TITAN and ILD 2 films and is within error of other reports.[109,119] When comparing the ZIF-8 film to an amorphous film of matched porosity (e.g., 60% porous TITAN), the MOF film exhibits much small pore sizes, a higher mechanical strength due to the structural order and rigidity of molecules, but a substantially higher *k*-value (likely due to the higher polarizabilities of the metal and aromatic ligands).

When compared to a porous amorphous SiCOH film of similar *k*-value (e.g., $k = 2.35$; ILD 2), the ZIF-8 film has slightly smaller pore sizes, a considerably higher porosity, and therefore a much lower mechanical strength.

While the ZIF-8 film clearly demonstrates that structural order at a given porosity can deliver higher mechanical strength and smaller pore sizes, our results highlight some instability in the crystalline grain boundaries and that electrical measurements for gas adsorbing media need to be measured in controlled environments. It will be exciting to see how

https://doi.org/10.1557/jmr.2015.313 Published online by Cambridge University Press

single-crystal MOF films of various compositions can address these challenges.

VII. PORE SIZE, POROSITY, AND BACKBONE WIDTH

Even while the PMO and ZIF-8 films clearly show how ordered films can deliver highly porous and uniquely strong networks with small pore sizes, there is a desire to make pore sizes increasingly smaller. A figure of merit is to have the pore size much smaller than the patterned trench size to limit line-edge roughness and other processing risks. As the critical dimensions of backend trench patterning is rapidly approaching the sizes near 10 nm, pore sizes of less than 1 nm are targeted. Figure 25 shows graphical representations of two networks of 56% porosity containing perfectly cut 12 nm wide trenches. Figure 25(a) shows random placement of 56% volume of pores on a molecularly-sized 1 nm square grid; this image therefore places the trench pitch, molecular size, and corresponding pore size on the same scale. One can visually see that the average pore size is larger than the porogen unit size because as the amount of porogen is increased, a given porogen molecule is more likely to have other porogen molecules as next nearest neighbors and therefore the

TABLE II. Data for various ILD materials: the ZIF-8 MOF, the randomly porous TITAN, and the PECVD ILD 2 material.

Material	Porosity (%)	Pore size (nm)	*E* (GPa)	*k*
TITAN	60	3.5–6	2.0	1.60
MOF	60[a]	0.3, 1[a]	2.7	2.35
ILD 2	30	1.5	7.0	2.35

[a]Porosity and pore sizes come from calculated values[16,120,121] and were not able to be experimentally verified.

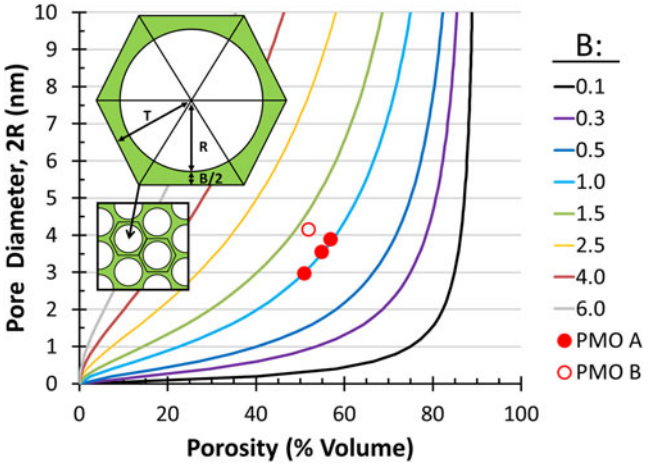


FIG. 26. Pore radius, *R*, to diameter, 2*R*, versus porosity and backbone width, *B*, for a porous material composed of a hexagonal packing of horizontally aligned cylindrical pores.

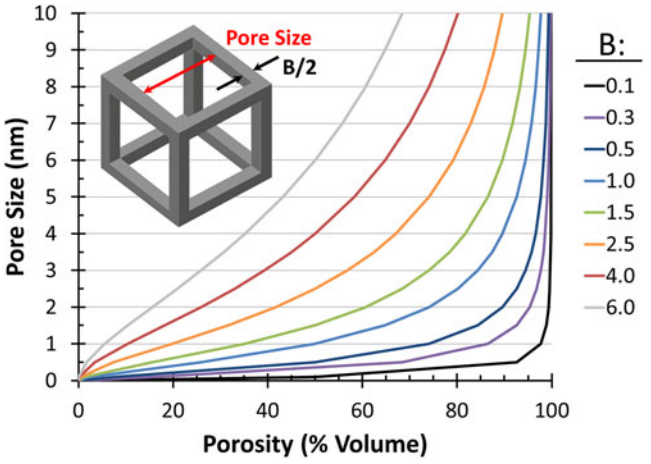


FIG. 27. Pore size versus porosity and backbone width, *B*, for a porous material composed of an idealized cube frame geometry.

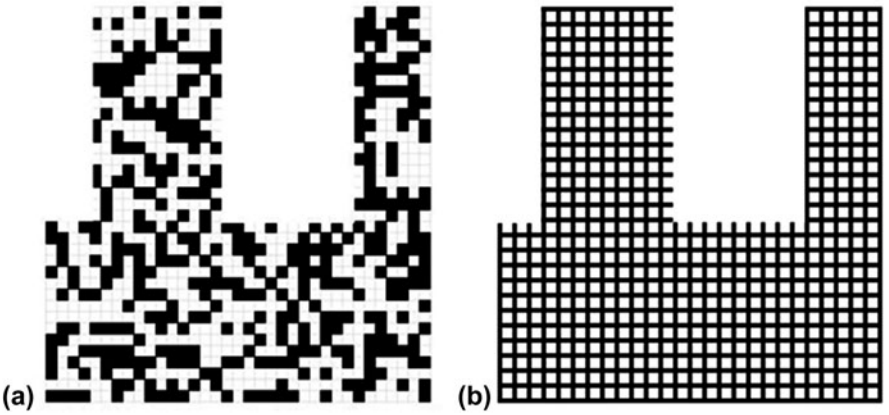


FIG. 25. Schematic models for a 12 nm half pitch integrated structure with super imposed representative porosity: (a) a randomly ordered 56% porous material containing an average unit size of 1 nm for both pore and backbone; (b) an ordered square lattice at 56% porosity with a closed 1 nm pore size and a 0.3 nm backbone wall width.

https://doi.org/10.1557/jmr.2015.313 Published online by Cambridge University Press

pore size of the total interconnected porogen phase increases. To limit the pore size of the material to the porogen unit size, porogen-porogen contact needs to be prevented by surrounding at least part of each porogen unit with backbone material. Figure 25(b) shows a hypothetically ordered structure comprising 1 nm square pores separated by a 0.3 nm wide backbone grid with an overall porosity of 56%. This structure represents pore sizes 3× smaller than the PMO material, and the width of the backbone unit is clearly on the atomic size scale (similar to the MOF materials).

The two structures of Fig. 25 hint at a trade-off between porosity, backbone width, and pore size, which can be calculated more explicitly using geometry for films exhibiting ordered structures of various types. The inset in Fig. 26 shows the hcp pore structure for PMOs and the 6 subunits making up one pore together with the dimensional variables used for calculation, where R is the pore radius and B is the backbone width. The porosity, P, is the ratio of the pore area ($A_{\text{pore}} = \pi R^2$) to the hexagonal unit cell area [$A_{\text{hexagon}} = 2 \times (3)^{0.5} \times \text{T}^2 = 2 \times (3)^{0.5} \times (\text{R} + \text{B}/2)^2$]. Notice that the porosity can be described only in terms of R and B. There are therefore only 2 independent variables between backbone width, porosity, and pore size. Figure 26 plots the pore radius versus porosity for a set of hypothetical cylindrical hcp PMO structures with defined backbone widths, B. Data for PMO materials are overlaid on the graph. The three PMO A films were synthesized using one type of molecular surfactant with three different organic chain lengths, and they clearly lie on one trend line that is fit by a backbone width of 1.0 nm. While the alkyl chain length of the surfactant determined the pore size, the similar head group resulted in the same number of organosilicate molecules around the micelle. In this case, we see the increase in radius giving an increase in porosity for the same backbone width. The PMO B film was generated using a molecular surfactant with a different head group relative to PMO A; this head group apparently facilitates the growth of a slightly thicker organosilicate shell, and therefore a thicker backbone width.

The experimental PMO data and geometrical models clearly demonstrate the challenge of scaling PMO materials to higher porosities: a 70% porous film with the same 1 nm backbone width would result in a 7 nm pore diameter. Alternatively, a 60% porous structure with pore diameter of 1 nm would require a potentially impractical 0.2 nm backbone width.

The hcp cylindrical pore geometry of Fig. 26 is not necessarily the best structure from either a mechanical (Figs. 13 and 20) or an optimal pore size perspective. A cube frame structure, if achievable to synthesize, would provide straight load paths upon mechanical stress and would better optimize for a larger backbone wall thickness for a given porosity and pore size. Figure 27 shows a representative unit cell for the cube fame structure along with the calculated geometrical constraints for porosity, backbone width, and pore size for a cube frame structure. Notice that a 60% porous cube frame structure with a 1 nm pore size would result in backbone width of roughly 0.7 nm; this is 3.5× thicker and hence more feasible than the hcp cylindrical pore structure. A 70% porous cube frame with 1 nm thick backbone walls would result in a pore size of less than 2 nm.

While we have not considered all possible geometric structures, the comparison between these two cases highlights some important considerations regarding the feasibility of scaling both porosity and pore size. Nevertheless, the schemes presented here provide a step toward developing new material design rules needed to enable simultaneous material porosity and pattern density scaling of backend interconnects.

VIII. CONCLUSIONS

ILD materials for extreme capacitance scaling will need to be carefully crafted. We demonstrate the importance of precursor design through the results of the in-house synthesized TITAN film, which was designed for mechanical strength, high porosity, and chemical stability. Carbon atoms added into the backbone of the molecule as Si–R–Si groups are typically more chemically stable than pendant methyl groups and do not reduce the coordination number of the backbone molecular unit. Backbone oligomers synthesized to have a high number of reactive crosslinking groups result in films with high mechanical strength at a given porosity. PT sets a limit on the maximum porosity achievable with randomly ordered porous networks; this maximum porosity can be increased by tuning the network coordination number of the backbone units. Ordered networks of controlled porosity can provide higher maximum porosity values and can deliver higher mechanical strength at a given porosity for certain pore geometries. There are geometrical limitations on the molecular backbone width when trying to scale ordered networks to high porosity and low pore size. While the integration of highly porous low-k materials like TITAN will require novel new schemes, initial patterning and e-test data of this film looks encouraging[125] and is the focus of further work. While chip manufacturers are ultimately responsible for the successful integration of new materials, a larger pipeline of highly porous and ordered materials will facilitate success. Our hope is that this work spurs more materials development in both academia and industry.

https://doi.org/10.1557/jmr.2015.313 Published online by Cambridge University Press

IX. SUPPORTING INFORMATION

A. Additional data

A table containing raw numbers for several films presented in this work is included below.

Film	Porosity (% Vol)	Thk (nm)	*E* (GPa)	E error (GPa)	*k*	*k* SD
TITAN	0.2	88.0	32.17	2.56	3.41	0.04
TITAN	18.5	95.9	25.04	1.99	3.01	0.02
TITAN	33.7	103.3	15.91	1.51	2.51	0.02
TITAN	42.1	105.9	10.53	1.58	2.25	0.03
TITAN	50.5	105.4	5.52	0.49	1.94	0.02
TITAN	59.7	107.1	3.27	0.56	1.73	0.01
TITAN	60.9	106.9	3.27	0.40	1.72	0.02
TITAN	62.0	117.0	2.59	0.38	1.63	0.02
TITAN	62.3	107.1	2.61	0.33	1.65	0.04
TITAN	59.7	106.8	2.30	0.49	1.62	0.01
TITAN	57.2	101.9	2.29	0.36	1.59	0.01
ILD 0	4.5	N/A	10.5	N/A	3.1	N/A
ILD 1	12.0	124.3	9.4	0.2	2.58	0.1
ILD 2	31.0	104.5	7	0.2	2.31	0.1
ILD 3	42.0	112.0	5.1	0.6	2	0.1

B. Experimental details

Unless otherwise specified, dielectric thin films were directly deposited on p-Si(100) wafers of 5–25 Ω cm resistivity via spin coating. The film thickness values were measured using VASE over a wave length range of 600–1000 nm using 10 nm steps at incidence angles of 60 and 75° off normal. Films were fit to a Cauchy model to extract thickness, *A*, and *B* values, where the RI at a given wave length, λ, in units of micrometers is given by $RI(\lambda) = A + B/(\lambda^2)$. All films of this work had $B < 0.01$ over this wave length range. Film thicknesses were corroborated by properly performed SEM analysis using a small beam current, low acceleration voltage, and small integration times to minimize film shrinkage.

Pore volumes (porosity values) of the thin films were measured using a commercially available ellipsometric porosimeter using solvents of either toluene, 2-propanol, or water by measuring the thickness and RI values of the films under vacuum and at pressure intervals up to the saturation vapor pressure of the solvent using a pressure step size of 1–2% of the saturation vapor pressure for each solvent. This level of pressure sampling resulted in good resolution of the pore size distributions. The porosity values obtained for toluene or 2-propanol were within 1% volume of each other.

Young's modulus values (assuming a Poisson's ratio of 0.17 for all films) were measured by nano-indentation using the continuous stiffness method using a Berkovich tip as described in the literature.[96–99] For the most accurate comparison, all films were within a narrow thickness range and measured on one of two toolsets where films with a wide range of modulus values yielded nominally matched results.

The dielectric constant, *k*, values of the TITAN films were measured on a Hg probe with a calibrated area of 0.022 ± 0.01 cm^2 at a measurement frequency of 100 kHz under accumulation voltage conditions. The average and standard deviation over 3 repeat measurements at each of 3–5 different regions on a wafer were calculated. ILD films coated on 200 or 300 mm Si(100) wafers were mounted on an electrically grounded chuck with a vacuum system to ensure good electrical contact. Film thicknesses were sufficiently thick to minimize errors from series resistances. To minimize the series resistances for smaller 2 × 2 in. coupons, accurate *k*-value measurement required low resistivity (0.005–0.01 Ω cm) silicon substrates and a custom thin metal plate to focus the chuck vacuum for good electrical contact. Electrical leakage values measured with the Hg probe were conducted by monitoring the current flow under application of 0 to −100 V with a step size of 1 V, a current auto-ranging function activated, and a compliance current of 0.5 mA. Electrical leakage measurements performed under air are very sensitive to amount of physisorbed moisture; small changes in the amount of water uptake (as measured by EP with water solvent) showed relative large changes in both the leakage at a given electrical field and the voltage value for electrical breakdown. Accurate comparison of the electrical properties of highly porous dielectric thin films is therefore very challenging in this respect and the corresponding electrical leakage currents measured in air are not a reliable predictor for the leakage currents observed in hermetically capped integrated patterned structures. Comparison of electrical leakage in air and vacuum required a probe station equipped with turbo and roughing pumps to obtain a base pressure in the 10^{-7} to 10^{-8} Torr range. 500 nm thick aluminum dots of 5 different radius values ranging from 0.2 to 1 mm were deposited on the ILD films deposited on low resistivity Si wafers using a shadow mask evaporation technique. Electrical leakage values were trusted when current density values scaled with dot area and not dot circumference or other function. The grounding probe was contacted directly with the Si substrate and confirmed to have less than 2 kΩ contact resistance. Contact of the other probe to the Al dot requires care—typical over-travel of the 25 μm tungsten probes during lowering was about 50 μm; larger over-travel values would more substantially scratch the Al dot and raise concerns about underlying ILD damage. After electrical breakdown of one dot, probes needed to be properly discharged/grounded prior to landing on a new dot. Due to the highly doped Si substrate, leakage currents could be measured for both negative and positive applied voltage under otherwise similar measurement conditions as described for the Hg probe. Electrical leakage currents measured in air for the Al dot structures were very similar

https://doi.org/10.1557/jmr.2015.313 Published online by Cambridge University Press

to the air measurements made on the Hg probe. Samples measured under vacuum were first annealed for 12 h at 127 °C under vacuum (at 10^{-6} Torr) followed by 8 h of cool down to 27 °C. Once cooled to 27 °C, good contact to the Si substrate was ensured prior to dot measurement. Porous films with pore sizes of several nanometers in size (e.g., TITAN) result in Al infiltration during metal dot deposition using evaporation and electric field enhancements and early dielectric breakdown due to the resulting rough interface between metal and ILD surface. These challenges prevent a fair comparison of the electrical leakage between ZIF-8 (really small pore size) and TITAN (larger pore size). When properly integrated, however, the electrical leakage measurements of TITAN on patterned structures provide the most reliable (and most encouraging) data.

ACKNOWLEDGMENTS

Kris Vanstreels and IMEC for nano indentation measurements. Han Li at Intel for nano-indentation and aDCB measurements. Mark Lemay and Eungnak Han for PMO patterning support. Brian Krist and Gaiying Yang for TEM support. Rami Hourani, Shane Harlson, Marie Krysak, Steve Putna, and Kent Frasure for chemical synthesis, deposition, and characterization work. Jeff Callipare, Jack Mitchell, Brian Barley, and Bob Hankel for film deposition, capacitance, and EP measurements. Mike Bowen for ALD support. Satyarth Suri for etch development work. Marc French for XRD support. Mike Terzich for SEM support. Jeff Bielefeld, Canay Ege, Sean King, Ebony Mays, David Collins, and Veronica Strong for helpful discussions and other support.

REFERENCES

1. ITRS 2013, http://www.itrs.net/ITRS%201999-2014%20Mtgs,%20Presentations%20&%20Links/2013ITRS/Summary2013.htm.
2. G.E. Moore: No exponential is forever: But "Forever" can be delayed![semiconductor industry]. In *IEEE International Solid-State Circuits Conference Digest of Technical Papers*, IEEE: 2003; p. 20.
3. G.E. Moore: Cramming more components onto integrated circuits. *Proc. IEEE* **86**(1), 82 (1998).
4. W. Volksen, R.D. Miller, and G. Dubois: Low dielectric constant materials. *Chem. Rev.* **110**(1), 56 (2010).
5. A. Husain: Models for interconnect capacitance extraction. In *International Symposium on Quality Electronic Design*, IEEE: 2001; p. 167.
6. K. Maex, M. Baklanov, D. Shamiryan, S. Brongersma, and Z. Yanovitskaya: Low dielectric constant materials for microelectronics. *J. Appl. Phys.* **93**(11), 8793 (2003).
7. K. Lionti, W. Volksen, T. Magbitang, M. Darnon, and G. Dubois: Toward successful integration of porous low-k materials: Strategies addressing plasma damage. *ECS J. Solid State Sci. Technol.* **4**(1), N3071 (2015).
8. M. Baklanov, P.S. Ho, and E. Zschech: *Advanced Interconnects for ULSI Technology* (Chicester: John Wiley & Sons, 2012).
9. A. Grill, V. Patel, K. Rodbell, E. Huang, M. Baklanov, K. Mogilnikov, M. Toney, and H-C. Kim: Porosity in plasma enhanced chemical vapor deposited SiCOH dielectrics: A comparative study. *J. Appl. Phys.* **94**(5), 3427 (2003).
10. T.C. Choy: *Effective Medium Theory: Principles and Applications* (New York: Oxford University Press, 1999).
11. S. King, M. French, J. Bielefeld, and W. Lanford: Fourier transform infrared spectroscopy investigation of chemical bonding in low-k a-SiC: H thin films. *J. Non-Cryst. Solids* **357**(15), 2970 (2011).
12. D. Mu, Z-S. Liu, C. Huang, and N. Djilali: Determination of the effective diffusion coefficient in porous media including Knudsen effects. *Microfluid. Nanofluid.* **4**(3), 257 (2008).
13. H-P. Müller, R. Kimmich, and J. Weis: NMR flow velocity mapping in random percolation model objects: Evidence for a power-law dependence of the volume-averaged velocity on the probe-volume radius. *Phys. Rev. E* **54**(5), 5278 (1996).
14. M. Sahimi: *Applications of Percolation Theory* (Boca Raton: CRC Press, Taylor & Francis Group, 1994).
15. M.P. Petkov, M.H. Weber, K.G. Lynn, and K.P. Rodbell: Probing capped and uncapped mesoporous low-dielectric constant films using positron annihilation lifetime spectroscopy. *Appl. Phys. Lett.* **77**(16), 2470 (2000).
16. W. Zhou, S. Bailey, R. Sooryakumar, S. King, G. Xu, E. Mays, C. Ege, and J. Bielefeld: Elastic properties of porous low-k dielectric nano-films. *J. Appl. Phys.* **110**(4), 043520 (2011).
17. H. Kim: The application of atomic layer deposition for metallization of 65 nm and beyond. *Surf. Coat. Technol.* **200**(10), 3104 (2006).
18. M.R. Baklanov, J-F. de Marneffe, D. Shamiryan, A.M. Urbanowicz, H. Shi, T.V. Rakhimova, H. Huang, and P.S. Ho: Plasma processing of low-k dielectrics. *J. Appl. Phys.* **113**(4), 041101 (2013).
19. M. Goldman, D. Graves, G. Antonelli, S. Behera, and J. Kelber: Oxygen radical and plasma damage of low-k organosilicate glass materials: Diffusion-controlled mechanism for carbon depletion. *J. Appl. Phys.* **106**(1), 13311 (2009).
20. O. Richard, F. Iacopi, H. Bender, and G. Beyer: Sidewall damage in silica-based low-k material induced by different patterning plasma processes studied by energy filtered and analytical scanning TEM. *Microelectron. Eng.* **84**(3), 517 (2007).
21. E. Kunnen, G. Barkema, C. Maes, D. Shamiryan, A. Urbanowicz, H. Struyf, and M. Baklanov: Integrated diffusion–recombination model for describing the logarithmic time dependence of plasma damage in porous low-k materials. *Microelectron. Eng.* **88**(5), 631 (2011).
22. M.A. Worsley, S.F. Bent, S.M. Gates, N.C.M. Fuller, W. Volksen, M. Steen, and T. Dalton: Effect of plasma interactions with low-κ films as a function of porosity, plasma chemistry, and temperature. *J. Vac. Sci. Technol., B* **23**(2), 395 (2005).
23. O. Louveau, C. Bourlot, A. Marfoure, I. Kalinovski, J. Su, G. Hills, and D. Louis: Dry ashing process evaluation for porous ULK films. *Microelectron. Eng.* **73–74**, 351 (2004).
24. K.J. Singh: Unique size-dependent challenges for BEOL cleans in the patterning of sub-20 nm features. In *Solid State Phenomena*, Vol. **195**, P. Mertens, M. Meuris, and M. Heyns, eds.; Zurich: Trans Tech Publications, 2013; p. 103.
25. J. Chawla, K. Singh, A. Myers, D. Michalak, R. Schenker, C. Jezewski, B. Krist, F. Gstrein, T. Indukuri, and H. Yoo: Patterning challenges in the fabrication of 12 nm half-pitch dual damascene copper ultra low-k interconnects. In *SPIE Advanced Lithography*, International Society for Optics and Photonics: 2014; p. 905404.
26. M. Darnon, T. Chevolleau, O. Joubert, S. Maitrejean, J.C. Barbe, and J. Torres: Undulation of sub-100nm porous dielectric structures: A mechanical analysis. *Appl. Phys. Lett.* **91**(19), 194103 (2007).

https://doi.org/10.1557/jmr.2015.313 Published online by Cambridge University Press

27. G. Stan, C.V. Ciobanu, I. Levin, H.J. Yoo, A. Myers, K.J. Singh, C. Jezewski, B. Miner, and S. King: Nanoscale buckling of ultrathin low-k dielectric lines during hard-mask patterning. *Nano Lett.* **15**(6), 3845–3850 (2015).
28. J.S. Chawla, R. Chebiam, R. Akolkar, G. Allen, C.T. Carver, J.S. Clarke, F. Gstrein, M. Harmes, T. Indukuri, C. Jezewski, B. Krist, H. Lang, A. Myers, R. Schenker, K.J. Singh, R. Turkot, and H.J. Yoo: Demonstration of a 12 nm-half-pitch copper ultralow-k interconnect process. In *IEEE International Interconnect Technology Conference (IITC)*, IEEE: 2013; p. 1.
29. K. Hamioud, V. Arnal, A. Farcy, V. Jousseaume, A. Zenasni, B. Icard, J. Pradelles, S. Manakli, P. Brun, and G. Imbert: 32 nm node BEOL integration with an extreme low-k porous SiOCH dielectric k = 2.3. *Microelectron. Eng.* **87**(3), 316 (2010).
30. M. Fayolle, G. Passemard, O. Louveau, F. Fusalba, and J. Cluzel: Challenges of back end of the line for sub 65 nm generation. *Microelectron. Eng.* **70**(2–4), 255 (2003).
31. O.R. Rodriguez, W.N. Gill, J.L. Plawsky, T.Y. Tsui, and S. Grunow: Study of Cu diffusion in porous dielectrics using secondary-ion-mass spectrometry. *J. Appl. Phys.* **98**(12), 123514 (2005).
32. M. Fayolle, V. Jousseaume, M. Assous, E. Tabouret, C. Le Cornec, P.H. Haumesser, P. Leduc, H. Feldis, O. Louveau, G. Passemard, and F. Fusalba: Cu/ULK integration using a post integration porogen removal approach. In *Proceedings of the IEEE 2004 International Interconnect Technology Conference*, IEEE: 2004; p. 208.
33. T. Frot, W. Volksen, S. Purushothaman, R. Bruce, and G. Dubois: Application of the protection/deprotection strategy to the science of porous materials. *Adv. Mater.* **23**(25), 2828 (2011).
34. T. Frot, W. Volksen, S. Purushothaman, R.L. Bruce, T. Magbitang, D.C. Miller, V.R. Deline, and G. Dubois: Post porosity plasma protection: Scaling of efficiency with porosity. *Adv. Funct. Mater.* **22**(14), 3043 (2012).
35. L. Zhang, R. Ljazouli, P. Lefaucheux, T. Tillocher, R. Dussart, Y.A. Mankelevich, J-F. de Marneffe, S. de Gendt, and M.R. Baklanov: Low damage cryogenic etching of porous organosilicate low-k materials using $SF_6/O_2/SiF_4$. *ECS J. Solid State Sci. Technol.* **2**(6), N131 (2013).
36. Y. Kayaba, H. Tanaka, T. Suzuki, K. Kohmura, and S.S. Ono: Selective formation of an ultra-thin pore seal on mesorporous low-k for a copper dual damascene structure. In *IEEE International Interconnect Technology Conference/Advanced Metallization Conference (IITC/AMC)*, IEEE: 2014; p. 261.
37. Y-B. Jiang, N. Liu, H. Gerung, J.L. Cecchi, and C.J. Brinker: Nanometer-thick conformal pore sealing of self-assembled mesoporous silica by plasma-assisted atomic layer deposition. *J. Am. Chem. Soc.* **128**(34), 11018 (2006).
38. B.K. Moon, T. Iijima, S. Malhotra, A. Simon, T. Shaw, T. Ryan, C. Labelle, N. Fuller, T. Bolom, D. Dunn, P. Flaitz, S. Mehta, K. Inoue, and V. McGahay: Integration of ALD-TaN Liners on nanoporous dielectrics. *MRS Online Proc. Libr.* **863**, 1–6 (2005).
39. W. Puyrenier, V. Rouessac, L. Broussous, D. Rébiscoul, and A. Ayral: Effect of plasma treatments on a porous low-k material—Study of pore sealing. *Microporous Mesoporous Mater.* **106**(1–3), 40 (2007).
40. L. Fu, M. Su, F. Kuechenmeister, and W. Huang: Chip package interaction (CPI) reliability of Cu/low-k/ultra-low-k interconnect. In *16th IEEE International Symposium on the Physical and Failure Analysis of Integrated Circuits*, IEEE: 2009; p. 691.
41. K. Mosig, T. Jacobs, K. Brennan, M. Rasco, J. Wolf, and R. Augur: Integration challenges of porous ultra low-k spin-on dielectrics. *Microelectron. Eng.* **64**(1–4), 11 (2002).
42. A. Grill: Plasma enhanced chemical vapor deposited SiCOH dielectrics: From low-k to extreme low-k interconnect materials. *J. Appl. Phys.* **93**(3), 1785 (2003).
43. V. Jousseaume, G. Rolland, D. Babonneau, and J.P. Simon: Influence of polymer porogens on the porosity and mechanical properties of spin coated ultra low k dielectrics. *Thin Solid Films* **517**(15), 4413 (2009).
44. A.M. Padovani, L. Rhodes, S.A.B. Allen, and P.A. Kohl: Chemically bonded porogens in methylsilsesquioxane I. Structure and bonding. *J. Electrochem. Soc.* **149**(12), F161 (2002).
45. W. Volksen, T.P. Magbitang, R.D. Miller, S. Purushothaman, S.A. Cohen, H. Nakagawa, Y. Nobe, T. Kokubo, and G.J. Dubois: A manufacturing grade, porous oxycarbosilane spin-on dielectric candidate with K ≤ 2.0. *J. Electrochem. Soc.* **158**(7), G155 (2011).
46. L. Favennec, V. Jousseaume, V. Rouessac, F. Fusalba, J. Durand, and G. Passemard: Porous extreme low κ (ELκ) dielectrics using a PECVD porogen approach. *Mater. Sci. Semicond. Process.* **7**(4–6), 277 (2004).
47. A.M. Urbanowicz, K. Vanstreels, P. Verdonck, D. Shamiryan, S. De Gendt, and M.R. Baklanov: Improving mechanical robustness of ultralow-k SiOCH plasma enhanced chemical vapor deposition glasses by controlled porogen decomposition prior to UV-hardening. *J. Appl. Phys.* **107**(10), 104122 (2010).
48. M. Seino, W. Wang, J.E. Lofgreen, D.P. Puzzo, T. Manabe, and G.A. Ozin: Low-k periodic mesoporous organosilica with air walls: POSS-PMO. *J. Am. Chem. Soc.* **133**(45), 18082 (2011).
49. B. Hatton, K. Landskron, W. Whitnall, D. Perovic, and G.A. Ozin: Past, present, and future of periodic mesoporous organosilicas—The PMOs. *Acc. Chem. Res.* **38**(4), 305 (2005).
50. P. Marsik, P. Verdonck, D. De Roest, and M.R. Baklanov: Porogen residues detection in optical properties of low-k dielectrics cured by ultraviolet radiation. *Thin Solid Films* **518** (15), 4266 (2010).
51. M.R. Baklanov, L. Zhao, E.V. Besien, and M. Pantouvaki: Effect of porogen residue on electrical characteristics of ultra low-k materials. *Microelectron. Eng.* **88**(6), 990 (2011).
52. A.M. Urbanowicz, K. Vanstreels, D. Shamiryan, S. De Gendt, and M.R. Baklanov: Effect of porogen residue on chemical, optical, and mechanical properties of CVD SiCOH low-k materials. *Electrochem. Solid-State Lett.* **12**(8), H292 (2009).
53. P. Verdonck, D. De Roest, S. Kaneko, R. Caluwaerts, N. Tsuji, K. Matsushita, N. Kemeling, Y. Travaly, H. Sprey, M. Schaekers, and G. Beyer: Characterization and optimization of porogen-based PECVD deposited extreme low-k materials as a function of UV-cure time. *Surf. Coat. Technol.* **201**(22–23), 9264 (2007).
54. A. Zenasni, V. Jousseaume, P. Holliger, L. Favennec, O. Gourhant, P. Maury, and G. Gerbaud: The role of ultraviolet radiation during ultralow k films curing: Strengthening mechanisms and sacrificial porogen removal. *J. Appl. Phys.* **102**(9), 094107 (2007).
55. H. Sinha, G.A. Antonelli, G. Jiang, Y. Nishi, and J.L. Shohet: Effects of vacuum ultraviolet radiation on deposited and ultraviolet-cured low-k porous organosilicate glass. *J. Vac. Sci. Technol., A.* **29**(3), 030602 (2011).
56. E. Mickler, L. Ching-Te, A.T. Krishnan, J. Changming, and J. Manoj: A charge damage study using an electron beam low k treatment. In *Proceedings of the IEEE 2004 International Interconnect Technology Conference*, IEEE: 2004; p. 190.
57. G. Kloster, T. Scherban, G. Xu, J. Blaine, B. Sun, and Y. Zhou: Porosity effects on low-k dielectric film strength and interfacial adhesion. In *Proceedings of the IEEE 2002 International Interconnect Technology Conference*, IEEE: 2002; p. 242.
58. T. Yoda, K. Fujita, H. Miyajima, R. Nakata, N. Miyashita, and N. Hayasaka: Properties of high-performance porous SiOC low-k film fabricated using electron-beam curing. *Jpn. J. Appl. Phys.* **44** (6R), 3872 (2005).

https://doi.org/10.1557/jmr.2015.313 Published online by Cambridge University Press

59. T. Owada, N. Ohara, H. Watatani, T. Kouno, H. Kudo, H. Ochimizu, T. Sakoda, N. Asami, Y. Ohkura, S. Fukuyama, A. Tsukune, M. Nakaishi, T. Nakamura, Y. Nara, and M. Kase: Advanced BEOL integration using porous low-k (k=2.25) material with charge damage-less electron beam cure technique. In *IEEE International Interconnect Technology Conference*, IEEE: 2009; p. 149.
60. G. Dubois, W. Volksen, T. Magbitang, M. Sherwood, R. Miller, D. Gage, and R. Dauskardt: Superior mechanical properties of dense and porous organic/inorganic hybrid thin films. *J. Sol-Gel Sci. Technol.* **48**(1–2), 187 (2008).
61. S-K. Min, B. Moon, H. Kim, and H-W. Rhee: Cyclodextrin-based reactive porogen for nanoporous ultra-low dielectrics. *Curr. Appl. Phys.* **11**(1), S313 (2011).
62. J.H. Yim, J.B. Seon, H.D. Jeong, L.S. Pu, M.R. Baklanov, and D.W. Gidley: Morphological control of nanoporous films by the use of functionalized cyclodextrins as porogens. *Adv. Funct. Mater.* **14**(3), 277 (2004).
63. M. Baklanov and K. Mogilnikov: Non-destructive characterisation of porous low-k dielectric films. *Microelectron. Eng.* **64** (1), 335 (2002).
64. B. Kim, J. Son, and M. Ko: The effect of porogen on physical properties in MTMS–BTMSE spin-on organosilicates. *J. Mater. Sci.* **42**(14), 5381 (2007).
65. P.T. Hurley, L.-S. Du, P.L. McDaniel, B.K. Peterson, S.J. Weigel, M.K. Haas, R.N. Vrtis, D. Sinatore, M.D. Bitner, and K.E. Theodorou: Formation of porous organosilicate glasses produced by PECVD and UV treatment. In *Materials, Processes, Integration and Reliability in Advanced Interconnect for Micro- and Nanoelectronics*, ed. Q. Lin, E.T. Ryan, W-L. Wu, D.Y. Yoon (Mater. Res. Soc. Symp. Proc. **990**; New York: Cambridge University Press, 2007), p. 3.
66. F. Iacopi, Y. Travaly, B. Eyckens, C. Waldfried, T. Abell, E.P. Guyer, D.M. Gage, R.H. Dauskardt, T. Sajavaara, K. Houthoofd, P. Grobet, P. Jacobs, and K. Maex: Short-ranged structural rearrangement and enhancement of mechanical properties of organosilicate glasses induced by ultraviolet radiation. *J. Appl. Phys.* **99**(5), 053511 (2006).
67. X. Guo, J.E. Jakes, M.T. Nichols, S. Banna, Y. Nishi, and J.L. Shohet: The effect of water uptake on the mechanical properties of low-k organosilicate glass. *J. Appl. Phys.* **114**(8), 084103 (2013).
68. M. Baklanov, K. Mogilnikov, V. Polovinkin, and F. Dultsev: Determination of pore size distribution in thin films by ellipsometric porosimetry. *J. Vac. Sci. Technol. B* **18**(3), 1385 (2000).
69. C. Licitra, R. Bouyssou, T. Chevolleau, and F. Bertin: Multi-solvent ellipsometric porosimetry analysis of plasma-treated porous SiOCH films. *Thin Solid Films* **518**(18), 5140 (2010).
70. G. Bonilla, T.M. Shaw, E.G. Liniger, S. Cohen, S.M. Gates, A. Grill, H. Shobha, C.J. Penny, and E.T. Ryan: Tailoring dielectric materials for robust BEOL reliability. In *IEEE International Reliability Physics Symposium (IRPS)*, IEEE: 2012; p. 3A.1.1.
71. M.R. Baklanov, K.P. Mogilnikov, and Q.T. Le: Quantification of processing damage in porous low dielectric constant films. *Microelectron. Eng.* **83**(11), 2287 (2006).
72. W. Puyrenier, V. Rouessac, L. Broussous, D. Rébiscoul, and A. Ayral: Characterization of the impact of plasma treatments and wet cleaning on a porous low k material. *Microelectron. Eng.* **83**(11–12), 2314 (2006).
73. D. Rébiscoul, B. Puyrenier, L. Broussous, D. Louis, and G. Passemard: Study of the post-etch cleaning compatibility with dense and porous ULK materials—Characterization of the process impact. *Microelectron. Eng.* **83**(11–12), 2319 (2006).
74. J. Noguchi: Dominant factors in TDDB degradation of Cu interconnects. *IEEE Trans. Electron Devices* **52**(8), 1743 (2005).
75. A. Bhanap, T. Ramos, A. Camarena, and A. Naman: Repairing process-induced damage to porous low-k ILDs by post-ash treatment. In *Proceedings of Advanced Metallization Conference*, G.W. Ray, T.S. Smy, T. Ohta, M. Tsujimura, eds.; MRS: 2003.
76. L. Broussous, W. Puyrenier, D. Rebiscoul, V. Rouessac, and A. Ayral: Porosity and structure evolution of a SiOCH low k material during post-etch cleaning process. *Microelectron. Eng.* **84**(11), 2600 (2007).
77. M. Jochen and E.B. James: An analytic model for atom diffusion and heterogeneous recombination in a porous medium. *J. Phys. D: Appl. Phys.* **39**(17), 3849 (2006).
78. M. Matyka, A. Khalili, and Z. Koza: Tortuosity-porosity relation in porous media flow. *Phys. Rev. E.* **78**(2), 026306 (2008).
79. S. Sugahara, K-i. Usami, and M. Matsumura: A proposed organic-silica film for inter-metal-dielectric application. *Jpn. J. Appl. Phys.* **38**(3R), 1428 (1999).
80. E.T. Ryan, S.M. Gates, A. Grill, S. Molis, P. Flaitz, J. Arnold, M. Sankarapandian, S.A. Cohen, Y. Ostrovski, and C. Dimitrakopoulos: Property modifications of nanoporous pSiCOH dielectrics to enhance resistance to plasma-induced damage. *J. Appl. Phys.* **104**(9), 094109 (2008).
81. N. Inoue, F. Ito, H. Shobha, S. Gates, E.T. Ryan, K. Virwani, N. Klvmko, A. Madan, L. Tai, E. Adams, S. Cohen, E. Liniger, C.K. Hu, Y. Mignot, A. Grill, and T. Spooner: UV cure impact on robust low-k with sub-nm pores and high carbon content for high performance Cu/low-k BEOL modules. In *IEEE International Interconnect Technology Conference (IITC)*, IEEE: 2013; p. 1.
82. S.M. Gates, G. Dubois, E.T. Ryan, A. Grill, M. Liu, and D. Gidley: Adjusting the Skeleton and pore structure of porous SiCOH dielectrics. *J. Electrochem. Soc.* **156**(10), G156 (2009).
83. K.-I. Usami, S. Sugahara, M. Kobayashi, K. Sumimura, T. Hattori, and M. Matsumura: Preparation and properties of silica films with higher-alkyl groups. *J. Non-Cryst. Solids.* **260**(3), 199–207 (1999).
84. F. Goethals, I. Ciofi, O. Madia, K. Vanstreels, M.R. Baklanov, C. Detavernier, P. Van Der Voort, and I. Van Driessche: Ultra-low-k cyclic carbon-bridged PMO films with a high chemical resistance. *J. Mater. Chem.* **22**(17), 8281 (2012).
85. C.J. Brinker and G.W. Scherer: *Sol-Gel Science: The Physics and Chemistry of Sol-gel Processing* (San Diego: Academic Press, 2013).
86. V. Jousseaume, L. Favennec, A. Zenasni, and O. Gourhant: Porous ultra low k deposited by PECVD: From deposition to material properties. *Surf. Coat. Technol.* **201**(22–23), 9248 (2007).
87. J-H. Yim, M.R. Baklanov, D.W. Gidley, H. Peng, H-D. Jeong, and L. Sun Pu: Pore structure of modified cyclic silsesquioxane thin films made porous using a cyclodextrins-based porogen. *J. Phys. Chem. B* **108**(26), 8953 (2004).
88. R. Zallen: *The Physics of Amorphous Solids, in the Physics of Amorphous Solids* (New York: John Wiley & Sons, Inc., 1983).
89. F. Ciaramella, V. Jousseaume, S. Maitrejean, M. Verdier, B. Remiat, A. Zenasni, and G. Passemard: Crosslinking impact of mesoporous MSQ films used in microelectronic interconnections on mechanical properties. *Thin Solid Films* **495**(1–2), 124 (2006).
90. O. Gourhant, G. Gerbaud, A. Zenasni, L. Favennec, P. Gonon, and V. Jousseaume: Crosslinking of porous SiOCH films involving Si–O–C bonds: Impact of deposition and curing. *J. Appl. Phys.* **108**(12), 124105 (2010).

https://doi.org/10.1557/jmr.2015.313 Published online by Cambridge University Press

91. N.J. Trujillo, Q. Wu, and K.K. Gleason: Ultralow dielectric constant Tetravinyltetramethylcyclotetrasiloxane films deposited by Initiated chemical vapor deposition (iCVD). *Adv. Funct. Mater.* **20**(4), 607 (2010).
92. A. Soleimani Dorcheh and M.H. Abbasi: Silica aerogel; synthesis, properties and characterization. *J. Mater. Process. Technol.* **199**(1–3), 10 (2008).
93. M.R. Baklanov, E. Kondoh, E.K. Lin, D.W. Gidley, H.J. Lee, K.P. Mogilnikov, and J.N. Sun: Comparative study of porous SOG films with different non-destructive instrumentation. In *Proceedings of the IEEE 2001 International Interconnect Technology Conference*, IEEE: 2001; p. 189.
94. N. Tajima, T. Ohno, T. Hamada, K. Yoneda, S. Kondo, N. Kobayashi, M. Shinriki, Y. Inaishi, K. Miyazawa, K. Sakota, S. Hasaka, and M. Inoue: Carbon-doped silicon oxide films with hydrocarbon network bonds for low-k dielectrics: Theoretical investigations. *Jpn. J. Appl. Phys.* **46**(9R), 5970 (2007).
95. G. Dubois, T. Magbitang, W. Volksen, E.E. Simonyi, and R.D. Miller: New spin-on oxycarbosilane low-k dielectric materials with exceptional mechanical properties. In *Proceedings of the IEEE 2005 International Interconnect Technology Conference*, IEEE: 2005: p. 226.
96. H. Li, Y. Lin, T.Y. Tsui, and J.J. Vlassak: The effect of porogen loading on the stiffness and fracture energy of brittle organosilicates. *J. Mater. Res.* **24**(01), 107 (2009).
97. K. Vanstreels, C. Wu, P. Verdonck, and M.R. Baklanov: Intrinsic effect of porosity on mechanical and fracture properties of nanoporous ultralow-k dielectrics. *Appl. Phys. Lett.* **101**(12), 123109 (2012).
98. K. Vanstreels, C. Wu, M. Gonzalez, D. Schneider, D. Gidley, P. Verdonck, and M.R. Baklanov: Effect of pore structure of nanometer scale porous films on the measured elastic modulus. *Langmuir* **29**(38), 12025 (2013).
99. K. Vanstreels, C. Wu, and M.R. Baklanov: Mechanical stability of porous low-k dielectrics. *ECS J. Solid State Sci. Technol.* **4**(1), N3058 (2015).
100. S. Takada, N. Hata, Y. Seino, N. Fujii, and T. Kikkawa: Dependences of Young's modulus of porous silica low dielectric constant films on skeletal structure and porosity. *J. Appl. Phys.* **100**(12), 123512 (2006).
101. A.M. Urbanowicz, K. Vanstreels, P. Verdonck, E. Van Besien, T. Christos, D. Shamiryan, S. De Gendt, and M.R. Baklanov: Effect of UV wavelength on the hardening process of porogen-containing and porogen-free ultralow-k plasma-enhanced chemical vapor deposition dielectrics. *J. Vac. Sci. Technol., B* **29**(3), 032201 (2011).
102. K. Landskron, B.D. Hatton, D.D. Perovic, and G.A. Ozin: Periodic mesoporous organosilicas containing interconnected $[Si(CH_2)]_3$ rings. *Science* **302**(5643), 266 (2003).
103. H. Fan, C. Hartshorn, T. Buchheit, D. Tallant, R. Assink, R. Simpson, D.J. Kissel, D.J. Lacks, S. Torquato, and C.J. Brinker: Modulus-density scaling behaviour and framework architecture of nanoporous self-assembled silicas. *Nat. Mater.* **6** (6), 418 (2007).
104. F.K. de Theije, A.R. Balkenende, M.A. Verheijen, M.R. Baklanov, K.P. Mogilnikov, and Y. Furukawa: Structural characterization of mesoporous organosilica films for ultralow-k dielectrics. *J. Phys. Chem. B* **107**(18), 4280 (2003).
105. W. Wang, D. Grozea, S. Kohli, D.D. Perovic, and G.A. Ozin: Water Repellent periodic mesoporous organosilicas. *ACS Nano* **5** (2), 1267 (2011).
106. A.W. Wills, D.J. Michalak, P. Ercius, E.R. Rosenberg, T. Perciano, D. Ushizima, R. Runser, and B.A. Helms: Block copolymer packing limits and interfacial reconfigurability in the assembly of periodic mesoporous organosilicas. *Adv. Funct. Mater.* **25**(26), 4120 (2015).
107. A. Bétard and R.A. Fischer: Metal–organic framework thin films: From fundamentals to applications. *Chem. Rev.* **112**(2), 1055 (2012).
108. Z. Wang, J. Liu, S. Grosjean, D. Wagner, W. Guo, Z. Gu, L. Heinke, H. Gliemann, S. Bräse, and C. Wöll: Monolithic, crystalline MOF Coating: An excellent patterning and photoresist material. *ChemNanoMat* **1**(5), 338–345 (2015).
109. S. Eslava, L. Zhang, S. Esconjauregui, J. Yang, K. Vanstreels, M.R. Baklanov, and E. Saiz: Metal-organic framework ZIF-8 films As low-κ dielectrics in microelectronics. *Chem. Mater.* **25** (1), 27 (2013).
110. A. Thomas: Functional materials: From hard to soft porous frameworks. *Angew. Chem., Int. Ed.* **49**(45), 8328 (2010).
111. A.P. Roberts and E.J. Garboczi: Computation of the linear elastic properties of random porous materials with a wide variety of microstructure. *Proc. R. Soc. Lond. A Math Phys. Sci.* **458**(2021), 1033 (2002).
112. A.R. Boccaccini and Z. Fan: A new approach for the Young's modulus-porosity correlation of ceramic materials. *Ceram. Int.* **23**(3), 239 (1997).
113. I.M. Gitman, H. Askes, and L.J. Sluys: Representative volume: Existence and size determination. *Eng. Fract. Mech.* **74**(16), 2518 (2007).
114. M. Ostoja-Starzewski: Material spatial randomness: From statistical to representative volume element. *Probabilist. Eng. Mech.* **21**(2), 112 (2006).
115. Z. Chen, X. Wang, F. Giuliani, and A. Atkinson: Microstructural characteristics and elastic modulus of porous solids. *Acta Mater.* **89**, 268 (2015).
116. P. Marsik, A.M. Urbanowicz, P. Verdonck, D. De Roest, H. Sprey, and M.R. Baklanov: Effect of ultraviolet curing wavelength on low-k dielectric material properties and plasma damage resistance. *Thin Solid Films* **519**(11), 3619 (2011).
117. M. Guan, W. Wang, E.J. Henderson, Ö. Dag, C. Kübel, V.S.K. Chakravadhanula, J. Rinck, I.L. Moudrakovski, J. Thomson, J. McDowell, A.K. Powell, H. Zhang, and G.A. Ozin: Assembling Photoluminescent silicon Nanocrystals into periodic mesoporous organosilica. *J. Am. Chem. Soc.* **134**(20), 8439 (2012).
118. G. Lu, O.K. Farha, W. Zhang, F. Huo, and J.T. Hupp: Engineering ZIF-8 thin films for hybrid MOF-based devices. *Adv. Mater.* **24**(29), 3970 (2012).
119. J.C. Tan, T.D. Bennett, and A.K. Cheetham: Chemical structure, network topology, and porosity effects on the mechanical properties of zeolitic imidazolate frameworks. *Proc. Natl. Acad. Sci. U. S. A.* **107**(22), 9938 (2010).
120. A. Demessence, C. Boissiere, D. Grosso, P. Horcajada, C. Serre, G. Ferey, G.J.A.A. Soler-Illia, and C. Sanchez: Adsorption properties in high optical quality nanoZIF-8 thin films with tunable thickness. *J. Mater. Chem.* **20**(36), 7676 (2010).
121. K.S. Park, Z. Ni, A.P. Côté, J.Y. Choi, R. Huang, F.J. Uribe-Romo, H.K. Chae, M. O'Keeffe, and O.M. Yaghi: Exceptional chemical and thermal stability of zeolitic imidazolate frameworks. *Proc. Natl. Acad. Sci. U. S. A.* **103**(27), 10186 (2006).
122. S. Hermes, F. Schröder, R. Chelmowski, C. Wöll, and R.A. Fischer: Selective nucleation and growth of metal−organic open framework thin films on patterned $COOH/CF_3$-terminated self-assembled monolayers on Au(111). *J. Am. Chem. Soc.* **127**(40), 13744 (2005).
123. H. Gliemann and C. Wöll: Epitaxially grown metal-organic frameworks. *Mater. Today* **15**(3), 110 (2012).
124. L. Heinke, M. Tu, S. Wannapaiboon, R.A. Fischer, and C. Wöll: Surface-mounted metal-organic frameworks for applications in sensing and separation. *Microporous Mesoporous Mater.* **216**, 200 (2015).
125. J.D. Bielefeld: Personal communication, 2015.

https://doi.org/10.1557/jmr.2015.313 Published online by Cambridge University Press